Detailed seismic imaging of the Mw 7.1 Ridgecrest earthquake rupture zone from data recorded by dense linear arrays

Hongrui Qiu[1], Yehuda Ben-Zion[2,3], Rufus Catchings[4], Mark R. Goldman[4], Amir A. Allam[5], and Jamison Steidl[4,6]

[1]Department of Earth, Environmental and Planetary Sciences, Rice University, Houston, TX, USA

[2]Department of Earth Sciences, University of Southern California, Los Angeles, CA, USA

[3]Southern California Earthquake Center, University of Southern California, Los Angeles, CA, USA

[4]U.S. Geological Survey, 345 Middlefield Road MS 977, Menlo Park, California 94025-3591 U.S.A

[5]Department of Geology and Geophysics, University of Utah, Salt Lake City, UT, USA

[6]Earth Research Institute, University of California, Santa Barbara, CA, USA

Corresponding author: Hongrui Qiu (hongruiq@rice.edu, qiuhonrui@gmail.com)

Key points:

- Several 1- to 2-km-wide low-velocity zones with more intensely damaged inner cores (0.5-1.5 km wide) are identified beneath each array
- An automated detector, based on peak ground velocities and durations of high amplitude *S* waves, identifies fault-zone trapped waves
- The results of this study show complex internal fault-zone structures that vary along rupture strike, in agreement the surface geology

Abstract

We analyze seismograms recorded by four arrays (B1-B4) with 100-m station spacing and apertures of 4-8 km that cross the surface rupture of the 2019 Mw7.1 Ridgecrest earthquake. The arrays extend from B1 in the northwest to B4 in the southeast of the surface rupture. Delay times between *P*-wave arrivals associated with ~1200 local earthquakes and four teleseismic events are used to estimate local velocity variations beneath the arrays. Both teleseismic and local *P* waves travel faster on the northeast than the southwest side of the fault for ~4.6% and ~7.5% beneath arrays B1 and B4, but the velocity contrast is less significant at arrays B2 and B3. We identify several 1- to 2-km-wide low-velocity zones with more intensely damaged inner cores beneath each array. The damage zone at array B4 generates fault-zone head, reflected, and trapped waves. An automated detector, based on peak ground velocities and durations of high-amplitude waves, identifies candidate fault-zone trapped waves (FZTWs) in a localized zone for ~600 earthquakes. Synthetic waveform modeling of averaged FZTWs, generated by ~30 events with high-quality signals, indicate that the trapping structure at array B4 has a width of ~300 m, depth of 3-5 km, *S*-wave velocity reduction of ~20% with respect to the surrounding rock, *Q*-value of ~30, and *S*-wave velocity contrast of ~4% across the fault (faster on the northeast side). The results show complex fault-zone internal structures that vary along fault strike, in agreement the surface geology (alternating playa and igneous rocks).

1. Introduction

The Mw 7.1 Ridgecrest earthquake of July 5, 2019 and the earlier Mw 6.4 event on July 4 in the southern part of the Walker Lane shear zone (Figure 1) were felt throughout southern California and produced a vigorous aftershock sequence. These events led to rapid deployments of seismic arrays across and around the Ridgecrest earthquake sequence (Catchings et al., 2020). Kinematic rupture processes of the Mw 6.4 and Mw 7.1 events, surface deformation, and properties of the aftershocks show complex patterns, with strong variations both along strike of the rupture zones and at depth (e.g., Chen et al., 2020; Cheng & Ben-Zion, 2020; Jia et al., 2020; Ross et al., 2019; Xu et al., 2020).

Data recorded by several dense arrays crossing the rupture zone of the Mw 7.1 earthquake can be used to derive high-resolution seismic information on the internal structure of the rupture zone. Detailed imaging of the structure associated with the rupture zone can provide important information on various topics, including initiation and arrest of ruptures (e.g., Aki, 1979; King, 1986), amplification of seismic waves (e.g., Kurzon et al., 2014; Rovelli et al. 2002; Spudich & Olsen, 2001), interactions of ruptures with fault zone properties (e.g., Ben-Zion & Huang 2002; Brietzke & Ben-Zion 2006; Huang et al., 2014), and properties of earthquake sequences (e.g., Thakur et al., 2020).

Analyses of seismic data recorded by arrays across fault and rupture zones have proven highly effective in imaging fault damage zones and bimaterial interfaces with unprecedented resolution (e.g., Cochran et al., 2009; Li et al., 1994; Lewis et al., 2005; Peng et al., 2003; Qin et al., 2018; Qiu et al., 2017; Share et al., 2017, 2019). In this study, we investigate the seismic and geometrical properties of the damage structure associated with the 2019 Mw 7.1 Ridgecrest earthquake, based on the data obtained from four dense linear seismic arrays (B1-B4; triangles in Figs. 1 and 2) located across segments of the rupture. Analyses of the arrival patterns of *P* waves from both teleseismic and local seismic events across each array helps to detect and constrain properties of velocity contrast across the fault and overall low-velocity zones related to substantial rock damage. We identified fault-zone trapped waves, with amplified motions associated with core damage zones that are sufficiently coherent to act as a waveguide, at some locations and inverted for average geometrical and seismic properties of the fault-zone waveguide.

In the following sections, we describe the deployment and data processing in section 2 and present the methodology and results on various aspects of the fault-zone structures from each observation in section 3. The imaging results from different phases and analyses are summarized and discussed in section 4. The results show overall complex fault-zone structures that vary along the rupture strike, in general agreement with the surface geology in the Ridgecrest area (alternating playa and igneous rocks; Jennings et al., 1997).

2. Data & basic processing

Four linear arrays, with about 100-m station spacing and apertures of 4-8 km (colored triangles in Fig. 1), were deployed across the surface rupture of the 2019 Mw 7.1 Ridgecrest earthquake (red star in Fig. 1). The arrays extended from B1 in the northwest to B4 in the southeast of the surface rupture (Fig. 2). In total, the B-arrays consisted of 248 Fairfield and SmartSolo sensors that recorded continuously at 500 Hz for about one-month period (7/12/2019-8/8/2019).

For teleseismic delay time analysis (Section 3.1), we use the Taup toolkit (Crotwell et al., 1999) and velocity model IASP91 (Kennett & Engdahl, 1991) for predictions of *P*-arrival time at each station. The employed teleseismic earthquakes have epicentral distances between 30-90°, depth > 50 km, and Mw > 6.0. Waveforms of the teleseismic arrivals were truncated according to the predicted arrival times. For analysis of local *P* waves (Section 3.2), we first extracted the seismic waveforms generated by ~1200 local events (within the red box in Fig. 1) at each station and used the catalog of Hauksson et al. (2012, extended to 2019) for locations. The mean and linear trend were removed from the waveforms, and a bandpass filter between 0.5 Hz and 20 Hz was applied. In the study of fault zone trapped waves (Section 3.3), the north-south and east-west components are rotated to a coordinate system parallel and perpendicular to the fault strike.

3. Analysis

We conducted three types of studies involving different signals and spatial scales to image several components of the fault-zone structure generated by the 2019 Mw 7.1 Ridgecrest earthquake at locations beneath the four linear arrays (Fig. 2): teleseismic delay-time analyses (DTA), local *P*-wave DTA, and analysis associated with FZTWs following the *S*-wave arrival. We describe the analyses below, starting with the large-scale structural features (e.g., velocity contrast across the fault) and progressing to inner fault-zone components.

3.1 Teleseismic delay time analysis

During the one-month deployment, teleseismic *P* waves with sufficient signal to noise ratios (SNR > 5) between 0.5 and 2 Hz are recorded for three events at array B1 (Fig. S1)

and four earthquakes at arrays B2-B4 (Figs. 3, S2, and S3). We do not investigate teleseismic *S* waves since they have SNR < 5.

3.1.1 Methodology

As shown in previous studies (e.g., Ozakin et al., 2012; Qiu et al., 2017), there are three contributing factors to travel-time delays observed on a linear array for a teleseismic arrival: the geometry between the incoming plane wave and the array, topography, and the crustal structure beneath the array. To obtain the travel-time delays due to local crustal structures, we first predict arrival time of the teleseismic *P*-wave for each station and event pair using the IASP91 model and assume the station is at the sea level. Then, teleseismic *P* waveforms are truncated 15 s before and 30 s after the predicted arrival time (e.g., 0 s in Fig. 3) and bandpass filtered between 0.5 and 2 Hz. By aligning the teleseismic *P* waves with respect to the corresponding predicted arrival time at each station, we remove the delay times associated with the non-vertical-incident angle of incoming waves.

To extract the robust arrival-time pattern of *P* waves recorded by an array for a specific teleseismic event, we first cross correlate waveforms within a narrow *P*-wave window (e.g., between the black dashed lines in Fig. 3) for every pair of stations *i* and *j*. Let $\tilde{t}_{ij}$ be the time delay corresponding to where the cross-correlation function reaches the maximum. The estimated *P*-wave arrival time at the *i*-th station is given by

$$\tilde{T}_i = \sum_{j=1}^{N} \tilde{t}_{ij} \Big/ N, \tag{1}$$

where *N* is the number of stations. The center of the narrow *P*-wave window is determined based on the array-mean envelope function (black curves in Fig. 3), and the peak frequency of the array-mean *P*-wave amplitude spectrum (bottom left inset of Fig. 3) is used to set the window width. To further enhance the *P*-wave signals, we apply another filter with narrower frequency band (black dashed lines in bottom left inset of Fig. 3) to the teleseismic data prior to the cross correlation.

Since the mean of the arrival time pattern $\tilde{T}$ has no significance for our imaging, we can remove the mean and effect of un-modeled topography from the teleseismic *P*-wave delay time T_i

$$T_i = \tilde{T}_i - \sum_{j=1}^{N} \tilde{T}_j \Big/ N - \Delta h_i / v_{\mathrm{corr}}, \quad (2)$$

where v_{corr} is the *P*-wave velocity (Vp) and $\Delta h_i = h_i - \sum_{j=1}^{N} h_j / N$ represents the relative topography, with h_i indicating the elevation at the *i*-th station (colors in Fig. 2).

3.1.2 Results

Figure 3 shows *P* waveforms (colors) truncated for the analyzed teleseismic events (top left panels) recorded at B4. The teleseismic *P* waveforms of each event are narrow bandpass filtered according to the array-mean amplitude spectrum (bottom left panels of Fig. 3). Coherent *P* arrivals, with different peak frequencies (red stars in bottom panels of Fig. 3), are observed crossing the array for the four events. Arrival time patterns $\tilde{T}$ after the correction for source-array geometry (red dashed curves in Fig. 3; eq. 1) are estimated via cross correlation of *P* waveforms within a narrow window (black dashed lines in Fig. 3). Although the frequency content of the *P* waveforms is different between events (Figs. 3 and S1-S3), the obtained arrival patterns are, in general, consistent (e.g., fast in the NE and slow in the SW underneath array B4 in Fig. 4d).

The teleseismic *P* arrival patterns $\tilde{T}$ estimated for each array is first averaged over all events (black curves in Fig. 4). Then the delay time due to array topography (colors in Fig. 2) is corrected from the mean $\tilde{T}$ by assuming two different Vp values: 2 km/s and 4 km/s (dashed curves in Fig. 4). Features of delay-time patterns associated with a velocity contrast across the fault and a low-velocity zone (Fig. 6 of Qiu et al., 2017) are both observed in the results after the topographic correction in Fig. 4. Delay-time patterns resolved at arrays B1 and B4 yield velocity contrasts across the fault, with the southwest block being slower (~0.2 s and ~0.3 s in Figs. 4a and 4d). Topographic corrections have minor effects on the resolved arrival-time patterns at both arrays (dashed curves in Figs. 4a and 4d).

The velocity contrast underneath array B2 is much weaker (< 0.06 s) with the same polarity (SW being slower) compared to those of arrays B1 and B4 and varies significantly with the Vp used in topographic correction (Fig. 4b). In addition, delay time patterns associated with two ~1-km-wide low velocity zones (with ~0.04 s maximum

time delay; Fig. 4b) are seen centered at about 2.5 km southwest and 0.5 km northeast of the midpoint of array B2 (green circles in Fig. 2b). We also find a weak velocity contrast across the fault and a ~1- to 2-km-wide low-velocity zone (with ~0.04 s maximum time delay) centered at ~0.5 km southwest of the B3 array midpoint (green circles in Fig. 2c). Different from the other three arrays, the polarity of the velocity contrast at B3 depends on the Vp used in the topographic correction, i.e. the southwest block is slightly faster when Vp is larger than 4 km/s and vice versa.

3.2 Local *P*-wave delay time analysis

P waves from local earthquakes recorded by the B-arrays are observed at higher frequencies (peaks at ~8 Hz; e.g., Fig. 5a) compared to those of teleseismic events (between 0.5-2 Hz; e.g., Fig. 3). Thus, higher resolution images of local fault zone structures can be achieved by analyzing arrival times of direct *P* waves from local earthquakes across each array.

3.2.1 Methodology

Compared with teleseismic arrivals, the effect of source-receiver geometry on *P* waves for local earthquakes recorded by an array require additional processing than does the plane wave correction used in section 3.1.1. In order to extract the variations in *P*-wave arrival times associated with local fault-zone structures, we first suppress the contributions from source-receiver geometry and topographic variations by normalizing the time axis of the *P* waveform recorded at *i*-th station for event *j* with its corresponding hypocenter distance H_{ij} (e.g., from Fig. 5a to 5b). *P*-wave picks, s_{ij} in units of slowness (e.g., stars in Figs. 5b and S4b-S6b), are then picked via the short-term-average/long-term-average (STA/LTA) algorithm (Allen, 1978) using waveforms within the slowness range of 0.15-0.25 s/km (to exclude the effect of *S* waves). *P*-wave picks with SNR less than 10 are not used, and events are excluded if less than 80% of the array shows good quality *P*-wave picks.

Considering the slowness values averaged over the entire array, $\bar{s}_j = \sum_{j=1}^{N} s_{ij}/N$ for the local event *j*, can vary significantly with focal depth and epicenter location (due to 3-D velocity structures); therefore, we use relative slowness, $\hat{s}_{ij} = s_{ij}/\bar{s}_j$ (e.g., Qiu et al.,

2017; Share et al., 2017) to characterize statistical features of the local-structure-related *P*-wave arrival pattern using all available events. We can also estimate the local-structure-related *P*-wave arrival pattern in delay time, Δt_{ij} for station *i* and event *j*, as

$$\Delta t_{ij} = \left(s_{ij} - \bar{s_j}\right) \cdot H_{ij}, \quad (3)$$

and analyze the delay time patterns statistically for all events.

3.2.2 Results

Figure 6 shows the results of statistical analysis on the local-structure-related *P*-wave arrival pattern in relative slowness (Figs. 6a, 6c, 6e, and 6g) and delay time (Figs. 6b, 6d, 6f, and 6h) using all available local events (Figs. 5c and S4c-S6c). Figure 6a illustrates the relative slowness patterns estimated at array B1 for 670 events as a histogram per station (vertical slice of gray pixels). The mean and standard deviation of all the relative slowness patterns are depicted as the red curve and error bars, respectively (Fig. 6a). The small error bars and confined width of histograms (dark gray colors in Fig. 6a) suggest that the mean relative slowness curve is representative of the patterns observed from all 670 events. Good agreement between the mean pattern (red curve) and the distribution of *P*-wave arrival patterns for all events (dark gray colors) is seen at arrays B1 and B4 for both relative slowness and delay time (Figs. 6a, 6b, 6g, and 6h). The histograms (dark gray colors in Figs. 6c-6f) are wider at arrays B2 and B3, indicating the variations in *P*-wave arrival patterns between events are larger. This is likely due to more complicated fault-zone structures (e.g., conjugate fault ruptures associated with the Mw 7.1 and Mw 6.4 Ridgecrest earthquakes; Fig. 1) beneath arrays B2 and B3, compared to those of arrays B1 and B4.

Consistent with the teleseismic *P*-wave arrival time pattern shown in Fig. 4, we observe the features of delays in local *P*-wave arrival time associated with fault-zone models that are characterized by a velocity contrast across fault and low-velocity zones. The effect of velocity contrast across fault in the observed arrival pattern is depicted as a smoothed step function (solid black curves in Fig. 6). The polarity of the velocity contrast is the same for arrays B1, B2, and B4, with the southwest block being slower, consistent with results of the teleseismic delay time analysis (Figs. 4a, 4b, and 4d). The arrival pattern estimated at the B3 array indicates a locally faster southwest block, in agreement

with results shown in Fig. 4c, assuming Vp ≥ 4 km/s for the topographic correction. The amplitudes of velocity contrast across the fault are 4.6% (or ~0.1 s), 0.8% (or ~0.02 s), 2% (or ~0.036 s), and 7.5% (or ~0.2 s) at the sites of arrays B1-B4, respectively, comparable to those estimated using teleseismic *P* waves (Fig. 4; Section 3.1.2).

Low-velocity zones that further delay the *P*-wave arrivals are also observed at each array, in addition to the pattern associated with velocity contrast across fault (black solid curves in Fig. 6). We outline the entire range of delay patterns related to the major low-velocity zones underneath each array, with green dashed lines in Fig. 6, whereas the red dashed lines characterize the core of these low-velocity zones that yield large time delays with relatively flat slopes. To better visualize the locations of these major low-velocity zones with respect to the array configuration, we depict the core and entire range of these zones in Figure 2 as red and green bars. Consistent with the teleseismic *P*-wave arrival patterns obtained at arrays B2 and B3 (Figs. 4b and 4c), we retrieve higher resolution images of low-velocity zones with comparable widths centered at similar locations, i.e. two ~1-km-wide low-velocity zones centered at ~2.5 km southwest to and ~0.5 km northeast of the midpoint of the B2 array and one ~2-km-wide low-velocity zone centered close to the midpoint of the B3 array. Moreover, delay patterns related to low-velocity zones are also observed in results of arrays B1 and B4 (Figs. 6b and 6h), which are missing from those of the teleseismic delay time analyses (Figs. 4a and 4d) that are dominated by signals of large-velocity contrast across fault. This is likely due to the lower frequency content of teleseismic *P* waves that can only provide low-resolution images of internal fault-zone structures.

3.3 Fault-zone trapped waves

A low-velocity fault-damage zone that is sufficiently uniform over a given distance can act as a waveguide and generate, in addition to delay times and motion amplification, trapped waves resulting from constructive interference of critically reflected phases within the waveguide (e.g., Ben-Zion & Aki 1990; Igel et al., 1997; Jahnke et al., 2002). Such waves have been observed at many locations, including the San Jacinto fault zone (e.g., Lewis et al., 2005; Qin et al., 2018; Qiu et al., 2017; Share et al., 2019; Wang et al., 2019), the Parkfield section of the San Andreas fault (e.g., Li et al., 1990; Lewis and Ben-

Zion, 2010; Ellsworth & Malin, 2011), and various other faults in California, Japan, Italy, Turkey, and other places. Catchings et al. (2016) used peak ground velocities of *P* and *S* waveforms recorded by cross-fault linear arrays to infer the location and width of the West Napa-Franklin fault zone. Similarly, we find fault-damage-zone-related amplification in data recorded by the B-arrays (e.g., Figs. 7 and S7) and use such amplification to detect FZTW candidates. In this section, we first infer the location and width of fault damage zones that produce FZTW using waveforms at the fault-parallel component, and then use waveforms of these candidates recorded by array B4 to invert for properties (e.g., width, velocity, attenuation) of the local fault-zone waveguide.

3.3.1 Methodology

Figure 7a shows *S* waveforms recorded on the fault-parallel component of array B4 for an example event (square in Fig. 1). Preprocessing steps (e.g., Ben-Zion et al., 2003; Fig. S6 of Qiu et al., 2017), including instrument response removal, integration to displacement seismogram, and convolution with $1/t^{1/2}$ (i.e. a point-source response to that of an equivalent *SH* line dislocation source; e.g., Igel et al., 2002; Vidale et al., 1985), are applied to the data prior to FZTW analyses. Clear resonance-wave packages with large amplitudes are found at a group of stations (stations B416-423; blue bar in Fig. 7a) in the southwest part of the array. Figure 7b displays distributions of peak ground velocities (PGV; red circles) and root mean squares (RMS; blue stars) of the fault-parallel-component *S* waveforms, normalized by the maximum value of the entire array. Large values of PGV and RMS are seen at stations with FZTW (blue bar in Fig. 7a), with considerably higher amplitudes than at the rest of the array. We estimate the likelihood of FZTW recorded by a station as the multiplication of PGV and RMS (black curve in Fig. 7b), normalized by the maximum value of the entire array for each event. FZTWs, observed consistently at a confined spatial range of the array, are captured by high likelihood values (red bar in Fig. 8), averaged over all analyzed events, and these FZTWs can be used to infer the location and width of the fault-zone waveguide.

Since FZTW are clearly observed in *S* waveforms recorded at stations B416-B423 of array B4 for the example event in Figure 7a, we can identify candidate events with similar good-quality FZTWs by cross correlating the fault-parallel-component *S*

waveforms recorded by stations B416-B423 for each event with those of the example event. The trapped waves of candidate events (stars in Fig. 9a) that yield cross correlation coefficients higher than 0.85 (e.g., red waveforms in Fig. 9b) are averaged (red waveforms in Fig. 9c) and inverted for properties (e.g., width, shear velocities, and attenuation) of the average fault-zone waveguide using a genetic inversion algorithm (e.g., Ben-Zion et al., 2003; Lewis et al., 2005; Qiu et al., 2017).

We test a total number of 10,000 models (50 generations and 200 models per generation) to obtain a good estimate of the fault-zone parameters in the inversion. Parameters of the best-fitting model and the 2,000 models (investigated in the last 10 generations) are extracted from the inversion. Because there are strong trade-offs between model parameters governing FZTWs (e.g., Ben-Zion, 1998; Jahnke et al., 2002; Peng et al. 2003), a successful inversion not only yields good waveform fits but also shows consistency between parameters of the best-fitting model and peaks of the probability density distributions of parameters developed in the last 10 generations. Additional details on the method can be found in section 3.4 of Qiu et al. (2017) and Ben-Zion et al. (2003).

3.3.2 Results

Figure 8 shows the distributions of FZTW likelihood values (background gray colors) as a function of station location, estimated at arrays B1-B4 for all events within the red box shown in Figure 1. The mean likelihood values are depicted in red, with error bars representing a range of two standard deviations. The group of stations with large mean likelihood values (> 0.4) are bounded by the red bar on the top of each panel in Figure 8, except in Figure 8c, where the stations are near the edge of array B3. Although not all stations within the low-velocity zones identified in Figure 6 (blue bars at the bottom of each panel in Fig. 8) yield high values of FZTW likelihood, locations of the candidate fault-zone waveguides (red bars in Fig. 8) are in good agreement with some of the low-velocity zones (blue bars in Fig. 8). This is consistent with detailed fault-zone studies at Parkfield (Lewis & Ben-Zion, 2010), the rupture zone of the 1992 Landers earthquake (Peng et al., 2003), and fault zones in Japan (Mamada et al. 2004; Mizuno et al. 2008). These studies showed that various sections of fault zones produce delay times and other

signals of damaged rocks but are either too heterogeneous or have significant segmentation between sources and receivers to generate trapped waves (e.g., Igel et al. 1997, 2002; Jahnke et al. 2002).

Not all analyzed events show FZTW likelihood patterns that are consistent with the averaged curve. To identify candidate events that show high FZTW likelihood values at the group of stations outlined by the red bars in Figure 8, we first cross-correlate the likelihood pattern measured from each event (e.g., black curve in Fig. 7b) with the mean (red curve in Fig. 8) for arrays B1, B2, and B4. Events with cross correlation coefficients higher than 0.95 are identified as strong FZTW candidates. More than 600 such candidate events are found in the recordings of array B4, and further candidate selection through waveform cross correlations (Section 3.3.1) indicate that 33 events (stars in Fig. 9a) produce high-quality FZTWs between stations B416-B423 (red waveforms in Fig. 9b). These high quality FZTW candidates (top inset of Fig. 9a) show a consistent source-receiver path, indicating the depth of the fault-zone waveguide is likely shallower than 5 km, and there is an optimal range of incident inclination angle for injecting seismic energy into the fault damage zone beneath array B4 (e.g., Fohrmann et al. 2004).

Compared to FZTW observed from each candidate event (e.g., Fig. 9b), the stacked recordings (red waveforms in Fig. 9c) yield much higher SNRs and can thus provide more reliable and robust estimations of the average fault-zone waveguide properties. Figure 10 presents the inversion results from modeling the stacked waveforms shown in Figure 9c (in red). The best fitting model yields good waveform fits (Fig. 10a) and suggests an average fault-zone waveguide with width of ~280 m, Q value of ~30, and *S*-wave velocity ~80% of the surrounding host rocks (black dots in Fig. 10b). The estimated propagation distance inside the waveguide is ~5.4 km. Because this includes a propagation component along-strike, it suggests a waveguide depth of ~3 km. The estimated average *S*-wave velocity in the host rock is ~4.1 km/s, with the northeast block being ~4.2% faster, consistent with results from the *P*-wave delay-time analysis at array B4 (~3% velocity contrast across the LVZ#5, with the northeast area being faster in Figures 6g and 6h). The parameters of fault-zone models from the last 10 generations (2,000 models) are marked as green dots in Fig. 10b, with the black curve indicating the corresponding probability density (i.e. frequency of each parameter value weighted by

the fitness values). Combined with the good waveform fits, the consistency between the best fitting parameters (black dots) and peaks of the probability density (black curve) suggests that the best-fitting model provides a robust estimate of properties for the average fault-zone waveguide.

In addition to FZTW, we detect clear fault-zone head waves (FZHWs) on stations B420 and B422 (Fig. S8), arriving ~0.1 s earlier than the direct *P* wave, as inferred from horizontal particle motion analysis modified from the method of Bulut et al. (2012). Because the differential time between the FZHW and *P* wave decreases significantly from northeast (B422) to southwest (B420) in a short distance (~0.1 km), the observed FZHW is likely traveling along a local interface that is associated with the edge of the damage zone (e.g., Qiu et al., 2017) on the northeast side (between stations B422 and B423). Similar FZTW and FZHW signals are also clearly observed in the data of array B2 (e.g., Fig. S9) but not for arrays B1 and B3.

It is interesting to note that we find clear reflected waves between *P* and *S* arrivals in waveforms recorded by B4 for more than 10 events located beneath the array (Fig. 11a). Figure 11b shows such reflection signals for an example M 2.6 event (circle in Fig. 11a). The reflection phases are visible at stations B423-B457 (green curve in Fig. 11b) and correlate well with the shape of the direct *P* wave but with the opposite first-motion polarity, as demonstrated in Figure 11c for station B431 (red waveform in Fig. 11c). It is hard to determine the existence of such reflected signals at stations B401-423 due to weak direct *P* waves, strong FZTWs, and *P*-coda waves. The high amplitudes and hyperbolic-shaped arrival times of the reflected phases indicate the velocity contrast interface is vertical and south to station B423. Considering that the first motion of the *P* wave is positive at stations on the southwest (red arrow) and negative on the northeast (blue arrow) in Figure 11b, the reversed polarity between the direct *P* and reflected waves suggests the observed phases of the example event are fault-zone reflected waves (FZRWs) that are generated by the velocity contrast across the boundary southwest of the damage zone (Najdahmadi et al., 2016). The fact that the reflected signal disappears northeast to station B457 suggests the waveguide only extends to a shallow depth, e.g., ~4 km assuming a homogenous solid northeast of the interface, comparable to the depth estimated from FZTW modeling (Fig. 10).

4. Discussion

We use arrival times of *P* waves from teleseismic and local earthquakes, and fault zone trapped waves (FZTW) recorded by four long-aperture (4-8 km) arrays (B1 to B4 from NE to SW) to infer internal components of the Mw 7.1 Ridgecrest earthquake rupture zone. *P*-wave-arrival picking is done automatically via waveform cross correlation and a STA/LTA algorithm for four teleseismic events and ~1200 local earthquakes, respectively. We first identified FZTW by estimating its likelihood at each station using peak ground velocities and root mean squares of the recorded *S* waveforms (Fig. 7) for each event. This enables systematic and objective FZTW analyses of large datasets (four arrays and ~1200 events; Fig. 8). Then, we identified a good FZTW template via visual inspection, and the template was used to detect candidates that produce FZTWs with sufficient quality through waveform cross correlations (Figs. 9a-b). FZTWs of all the selected candidates are stacked (Fig. 9c) and inverted for fault-zone properties beneath array B4 (Fig. 10). These procedures lead to identification of ~600 broadly distributed events that produce consistently amplified *S* waveforms at stations B416-B423 and ~30 earthquakes with high-quality FZTWs that we used in the inversion.

P-wave delay times from both teleseismic and local earthquakes, after proper corrections for propagation and topography effects, show clear and consistent velocity contrasts across the fault, with the northeast side being faster at arrays B1 (~0.1 s; Figs. 4a and 6b) and B4 (~0.2 s; Figs. 4d and 6h). The arrival patterns of teleseismic *P* waves observed at arrays B2 (Fig. 4b) and B3 (Fig. 4c) are dominated by travel-time delays associated with low-velocity zones that are consistent with results determined from the local *P* waves (~0.04 s in Fig. 6d and ~0.02 s in Fig. 6f). This consistency between results obtained from *P* waves at different frequencies (from 0.7 Hz to 8 Hz) is an indication of the robustness of the inferred fault-zone structures. Although the delay times obtained from teleseismic *P* waves are generally consistent with results from local earthquakes, the patterns are spatially smoother and less robust, due to the lower frequency *P* waves and stacking of results from an insufficient number of teleseismic events. Therefore, we only

421 focus on the delay-time patterns obtained from local *P* waves (Section 3.2; Fig. 6) in this
422 section.

423 Figure 12a summarizes all fault zone imaging results from the four linear arrays with
424 an overlay of the surface geology map in the Ridgecrest region. The velocity contrast
425 across the fault, inferred from local *P* wave delay time analysis (Section 3.2; Fig. 6)
426 beneath each array (red circles), is labeled in both percentage (in blue) and seconds (in
427 red). The velocity contrast is much smaller (~1-2%) and reverses its polarity from B2 to
428 B3 over a short distance (< 5 km) along the fault strike. This is consistent with the
429 complicated surface geology (i.e. mixture of sediments and granitic rocks) and fault
430 surface traces (i.e. conjugate fault ruptures of the Mw 6.4 and Mw 7.1 Ridgecrest
431 earthquakes) beneath the two arrays. The results beneath array B3 may represent the
432 velocity contrast across the rupture zone of the Mw 6.4 event, which separates the
433 northwest block (with higher velocities) from the lower velocity block on the southeast,
434 rather than that of the Mw 7.1 mainshock. Because velocity contrasts across faults are
435 measured in both ratio (δ) and delay time (Δt), we can estimate the depth of the velocity
436 contrast, *h*, by the following equation:

$$h = \bar{V_p} \cdot \Delta t / \delta, \quad (4)$$

437 if $\delta^2 \ll 1$. Here, $\bar{V_p}$ is the average *P*-wave velocity in the upper crust. Figure 12b shows
438 the histogram of average Vp ($= 1/\bar{s_j}$ for event *j* in Section 3.2.1; i.e. array-mean *P*-wave
439 velocity averaged over the source-receiver path) of source-array pairs between all local
440 earthquakes and four arrays. The median of the histogram indicates $\bar{V_p} \approx 5.6$ km/s, and
441 thus, it suggests a consistent depth *h* of ~10-15 km beneath all four arrays following
442 Equation 4.

443 The major low-velocity zones found in Figure 6 are also marked in Figure 12a with
444 the red and green bars covering the core and the entire range of the damage zone. Good
445 agreements between locations of these low-velocity zones, the group of stations with
446 amplified *S* waveforms (red bars in Fig. 8), and fault surface traces (or their
447 extrapolations) are found beneath all four arrays, suggesting the damage zones are
448 associated with the Mw 7.1 Ridgecrest earthquake rupture and perhaps past ones. The
449 measurements of the maximum time delays associated with these low-velocity zones
450 (Figs. 6b, 6d, 6f, and 6h) can be used to evaluate the quality of Vp models beneath these

linear arrays (e.g., White et al., 2020). The sections of damage zones that generate high-quality FZTWs at B2 and B4 are outlined by blue lines in Figure 12a, whereas the red dashed lines denote the local velocity contrast interfaces that produce clear FZHW at stations on the southwest side (red arrows). Waveform modeling of FZTWs detected at array B4 yields good waveform fits and an average waveguide with fault-zone parameters comparable to those inferred from previous studies in SJFZ (Qin et al., 2018; Qiu et al., 2017; Share et al., 2017, 2019): width of ~300 m, Q of ~30, *S*-wave velocity reduction of ~20% inside the damage zone, and depth of 3-5 km (Fig. 10). We note that the trapping structure beneath array B4 locates at the southwest edge of the core low-velocity zone (red bar in Fig. 12a), likely indicative of a flower-shape damage zone (i.e. width decreases with depth) that is offset to the northeast.

Symmetry properties of fault damage zones with respect to the main slip surface can provide information on the statistically preferred direction of earthquake ruptures (e.g., Ben-Zion & Shi, 2005; Dor et al., 2006a; Mitchell et al., 2011; Xu et al., 2012). Preferred rupture direction is expected for prominent bimaterial faults (e.g., Ampuero & Ben-Zion, 2008; Andrews and Ben-Zion, 1997; Shlomai & Finberg, 2016; Weertman, 1980), which is not the case for the structure associated with the Ridgecrest mainshock. To examine symmetry properties of the damage zone associated with the Ridgecrest rupture, we compare fault surface traces (Figs. 2 and 12) with the location and width of each LVZ identified by delay time analysis (Fig. 6 and red bars in Fig. 2), *S*-wave amplification (Fig. 8), and observed FZTWs (Figs. 7a and S9b). The results can be summarized as follows.

In Figure 12, LVZ #1 and #2 are on the southwest (slower) side to the surface trace of the main rupture zone (thick line) and centered on past surface displacements mapped before the 2019 Ridgecrest earthquake (thin lines). These two LVZs are likely associated with past ruptures and distributed symmetrically relative to the surface trace of the fault, both in terms of location (Fig. 12) and width, as inferred from *S*-wave amplification (red bars in Fig. 8). LVZ #4 beneath array B3 is between the surface traces of the Mw 7.1 and Mw 6.4 events, so the damage zone at this location also does not have clear signatures of asymmetry. LVZ #3 is likely associated with an extrapolation of surface rupture of the Mw 7.1 earthquake, and it is located on the northeast (faster) side of the extrapolated

surface trace (Figs. 2b and 12). LVZs #5 and #6 beneath array B4 (red bars in Fig. 2d) are centered on the fault surface traces, but the southwest parts of these LVZs show higher amplification of *S* waves (Fig. 8d), which is indicative of asymmetric rock damage offset to the northeast (faster side). The LVZs that have clear FZTW also show mixed signals of damage asymmetry. LVZ #5 shows an asymmetric distribution of the damage zone offset to the faster crustal block (Fig. 12), while the trapping structure in LVZ #2 (Fig. S9b) is distributed symmetrically relative to the surface fault trace, as mentioned above (Figs. 2b and 8b). The mixed results on asymmetry properties of rock damage are in marked contrast to the strong damage asymmetry inferred for the San Jacinto and San Andreas faults in southern California (Dor et al., 2006a, 2006b; Lewis et al., 2005; Qin et al. 2018; Qiu et al., 2017; Share et al., 2019; Wechsler et al., 2009), North Anatolia fault in Turkey (Dor et al., 2008), and Arima-Takatsuki Tectonic Line in Japan (Mitchell et al., 2011).

In addition to FZTWs and FZHWs, we find clear FZRWs likely reflected from the southwest edge of the fault-zone waveguide (Fig. 11). Figure 12c shows the distribution of events generating FZRWs (circle and stars) in the cross section along array B4 (triangles). The hypothesized reflection interface is labeled and depicted as the long black line located at the boundary southwest to the damage zone (red bar), whereas the local interface that produces FZHWs is illustrated as the short black line at the northeast edge of the waveguide. Schematic ray paths of the direct *P* waves and FZRWs from an example event to station B431 (red triangle) are demonstrated in Figure 12c as blue and red arrows, respectively, with color representing the polarity of the *P*-wave first motion (blue – negative, red – positive).

Analyses of properties of FZRWs, such as amplitudes and arrival times with respect to those of the direct *P* waves, can improve the constraints on the depth of the fault zone (green ray path in Fig. 12c) and can help to image of the velocity contrast interface southwest of the fault-zone waveguide. Additional analysis of FZRWs in the data set examined in this paper may be the subject of a follow-up study. Combining the imaging results of this paper with local earthquake tomography, using data generated by aftershocks of the Ridgecrest mainshock (White et al., 2020), will provide detailed, multi-scale seismic velocity models for the Ridgecrest rupture zone and the surrounding area.

5. Conclusions

The rupture zone of the Mw 7.1 Ridgecrest earthquake is shown to have heterogeneous structures with significant along-strike variations in local damage zones, in agreement with the surface geology and fault surface traces in the Ridgecrest region.

Seismic velocity contrasts, ranging from 1%-7.5% in Vp across the rupture zone of the Mw 7.1 Ridgecrest earthquake, extend to depths of ~10-15 km, with the northeast being locally faster and well-captured by delay times of *P* waves from both teleseismic and local earthquakes recorded by arrays B1, B2, and B4. Array B3, crossing the surface ruptures of both the Mw 6.4 and Mw 7.1 events, likely detects an ~2% velocity contrast in Vp across the fault that hosted the Mw 6.4 earthquake, with the northwest side being higher in velocity.

Low-velocity zones (LVZ) that further delay the *P* waves of local seismic events are centered on mapped surface traces of faults. Significant amplification is seen consistently in *S* waveforms recorded at stations within some of the identified LVZ. Clear FZTW are identified at arrays B2 and B4, and inversion of high-quality FZTWs at array B4 indicates an average waveguide comparable to previous studies in the SJFZ. Phases identified as FZHWs and FZRWs, associated with the northeast and southwest boundaries of the fault zone waveguide, are observed at array B4 and can provide additional constraints on internal structures of the local fault zone. The rock damage in the six LVZs identified from delay-time analysis, amplification of waves, and observed FZTWs show a mixture of symmetrically distributed damage relative to the surface fault trace, with some signatures of asymmetry.

Data Availability

The digital data are available in mseed day volume format, with each component in a separate volume. The data samples are 4 byte floats and consistently sampled at 500 samples/second. Data described in this report are available from the IRIS Data Management Center (https://ds.iris.edu/ds/nodes/dmc/data/). An accompanying report for data acquisition is available from Catchings et al. (2020).

Acknowledgements

The rapid seismic deployment of nodes for the 2019 Ridgecrest earthquake sequence was partially supported by the U.S. Geological Survey, the Southern California Earthquake Center, and the National Science Foundation (grant EAR-1945781). Personnel from the USGS, University of California - Santa Barbara, University of Utah, University of Southern California, and the Naval Air Weapons Station (NAWS) – China Lake, including Elizabeth Berg, Joanne Chan, Coyn Criley, Garet Huddleston, Daniel Langermann Zhenning Ma, Andrew Madsen, Adrian McEvilly, Daniel Mongovin, and Jordan Wang, were invaluable in the rapid response. We thank IRIS-PASSCAL for providing 162 Fairfield Zland 3C nodes and Sandia National Laboratory for providing 54 Fairfield 3C nodes, and the USGS for providing 245 SmartSolo 3C nodes. We thank Josh Bain, Stephan Bork, Kyle Buck, Darrin Clodt, John Foster, Allen Grossardt, Cyndy Hopkins, Hugh Jones, T.J. Larson, James Lovern, Sean Oleary, Nancy Pahr, Mike Pierce, Jacob Rivera, Vince Wallace, and Shane Williams of the NAWS-China Lake for access and field assistance. We thank Kate Scharer for coordination assistance with the NAWS. The research done in this paper was supported by the National Science Foundation (Award EAR-1945781), the U.S. Department of Energy (Award #DE-SC0016520), and the Southern California Earthquake Center (based on NSF Cooperative Agreement EAR-1600087 and USGS Cooperative Agreement G17AC00047).

References

Aki, K. (1979). Characterization of barriers on an earthquake fault. *Journal of Geophysical Research*. https://doi.org/10.1029/JB084iB11p06140

Allen, R. (1978). Automatic earthquake recognition and timing from signal traces. *Bulletin of the Seismological Society of America*. 68 (5):1521-1532.

Ampuero, J. P., & Ben-Zion, Y. (2008). Cracks, pulses and macroscopic asymmetry of dynamic rupture on a bimaterial interface with velocity-weakening friction. *Geophysical Journal International*, *173*(2), 674–692. https://doi.org/10.1111/j.1365-246X.2008.03736.x

Andrews, D. J., & Ben-Zion, Y. (1997). Wrinkle-like slip pulse on a fault between different materials. *Journal of Geophysical Research B: Solid Earth*. https://doi.org/10.1029/96jb02856

Ben-Zion, Y. (1998). Properties of seismic fault zone waves and their utility for imaging low-velocity structures. *Journal of Geophysical Research: Solid Earth*. https://doi.org/10.1029/98jb00768

Ben-Zion, Y., & Aki, K. (1990). Seismic radiation from an SH line source in a laterally heterogeneous planar fault zone. *Bulletin - Seismological Society of America*.

Ben-Zion, Y., & Huang, Y. (2002). Dynamic rupture on an interface between a compliant fault zone layer and a stiffer surrounding solid. *Journal of Geophysical Research*. https://doi.org/10.1029/2001jb000254

Ben-Zion, Y., & Shi, Z. (2005). Dynamic rupture on a material interface with spontaneous generation of plastic strain in the bulk. *Earth and Planetary Science Letters*. https://doi.org/10.1016/j.epsl.2005.03.025

Ben-Zion, Y., Peng, Z., Okaya, D., Seeber, L., Armbruster, J. G., Ozer, N., et al. (2003). A shallow fault-zone structure illuminated by trapped waves in the Karadere-Duzce branch of the North Anatolian Fault, western Turkey. *Geophysical Journal International*. https://doi.org/10.1046/j.1365-246X.2003.01870.x

Brietzke, G. B., & Ben-Zion, Y. (2006). Examining tendencies of in-plane rupture to migrate to material interfaces. *Geophysical Journal International*. https://doi.org/10.1111/j.1365-246X.2006.03137.x

Bulut, F., Ben-Zion, Y., & Bohnhoff, M. (2012). Evidence for a bimaterial interface along the Mudurnu segment of the North Anatolian Fault Zone from polarization analysis of P waves. *Earth and Planetary Science Letters*. https://doi.org/10.1016/j.epsl.2012.02.001

Catchings, R. D., Goldman, M. R., Li, Y. G., & Chan, J. H. (2016). Continuity of the west napa-franklin fault zone inferred from guided waves generated by earthquakes following the 24 august 2014 Mw 6.0 south napa earthquake. *Bulletin of the Seismological Society of America*. https://doi.org/10.1785/0120160154

Catchings, R. D., M.R. Goldman, J.H. Steidl, J.H. Chan, A.A. Allam, C.J. Criley, Z. Ma, D.S. Langermann, G.J. Huddleston, A.T. McEvilly, D.D. Mongovin, E.M. Berg, and Y. Ben-Zion, 2020. Nodal Seismograph Recordings of the 2019 Ridgecrest Earthquake Sequence, *Seism. Res. Lett.*, doi: 10.1785/0220200203.

Chen, K., Avouac, J. P., Aati, S., Milliner, C., Zheng, F., & Shi, C. (2020). Cascading and pulse-like ruptures during the 2019 Ridgecrest earthquakes in the Eastern California Shear Zone. *Nature Communications*, *11*(1), 3–10. https://doi.org/10.1038/s41467-019-13750-w

Cheng, Y. and Y. Ben-Zion, 2020. Variations of earthquake properties before, during and after the 2019 M7.1 Ridgecrest, CA, earthquake, *Geophys. Res. Lett.*, 47, e2020GL089650, doi: 10.1029/2020GL089650.

Cochran, E., Li, Y. G., Shearer, P. M., Barbot, S., Fialko, Y., & Vidale, J. E. (2009). Seismic and geodetic evidence for extensive, long-lived fault damage zones. *Geology*. https://doi.org/10.1130/G25306A.1

Crotwell, H. P., Owens, T. J., & Ritsema, J. (1999). The TauP Toolkit: Flexible Seismic Travel-time and Ray-path Utilities. *Seismological Research Letters*. https://doi.org/10.1785/gssrl.70.2.154

Dor, O., Rockwell, T. K., & Ben-Zion, Y. (2006a). Geological observations of damage asymmetry in the structure of the San Jacinto, San Andreas and Punchbowl faults in Southern California: A possible indicator for preferred rupture propagation direction. *Pure and Applied Geophysics*. https://doi.org/10.1007/s00024-005-0023-9

Dor, O., Ben-Zion, Y., Rockwell, T. K., & Brune, J. (2006b). Pulverized rocks in the Mojave section of the San Andreas Fault Zone. *Earth and Planetary Science Letters*. https://doi.org/10.1016/j.epsl.2006.03.034

Dor, O., Yildirim, C., Rockwell, T. K., Ben-Zion, Y., Emre, O., Sisk, M., & Duman, T.

Y. (2008). Geological and geomorphologic asymmetry across the rupture zones of the 1943 and 1944 earthquakes on the North Anatolian Fault: Possible signals for preferred earthquake propagation direction. *Geophysical Journal International*. https://doi.org/10.1111/j.1365-246X.2008.03709.x

Ellsworth, W. L., & Malin, P. E. (2011). Deep rock damage in the san andreas fault revealed by P- and S-type fault-zone-guided waves. *Geological Society Special Publication*. https://doi.org/10.1144/SP359.3

Fohrmann, M., Igel, H., Jahnke, G., & Ben-Zion, Y. (2004). Guided waves from sources outside faults: An indication for shallow fault zone structure? *Pure and Applied Geophysics*. https://doi.org/10.1007/s00024-004-2553-y

Hauksson, E., Yang, W., & Shearer, P. M. (2012). Waveform relocated earthquake catalog for Southern California (1981 to June 2011). *Bulletin of the Seismological Society of America*. https://doi.org/10.1785/0120120010

Huang, Y., Ampuero, J. P., & Helmberger, D. V. (2014). Earthquake ruptures modulated by waves in damaged fault zones. *Journal of Geophysical Research: Solid Earth*. https://doi.org/10.1002/2013JB010724

Igel, H., Ben-Zion, Y., & Leary, P. C. (1997). Simulation of SH- and P-SV-wave propagation in fault zones. *Geophysical Journal International*. https://doi.org/10.1111/j.1365-246X.1997.tb05316.x

Igel, H., Jahnke, G., & Ben-Zion, Y. (2002). Numerical simulation of fault zone guided waves: Accuracy and 3-D effects. *Pure and Applied Geophysics*. https://doi.org/10.1007/s00024-002-8724-9

Jahnke, G., Igel, H., & Ben-Zion, Y. (2002). Three-dimensional calculations of fault-zone-guided waves in various irregular structures. *Geophysical Journal International*. https://doi.org/10.1046/j.1365-246X.2002.01784.x

Jennings, C.W., Strand, R.G., and Rogers, T.H., 1977, Geologic map of California: California Division of Mines and Geology, scale 1:750,000.

Jia, Z., Wang, X., & Zhan, Z. (2020). Multifault models of the 2019 Ridgecrest sequence highlight complementary slip and fault junction instability. *Geophysical Research Letters*. https://doi.org/10.1029/2020GL089802

Kennett, B. L. N., & Engdahl, E. R. (1991). Traveltimes for global earthquake location and phase identification. *Geophysical Journal International*. https://doi.org/10.1111/j.1365-246X.1991.tb06724.x

King, G. C. P. (1986). Speculations on the geometry of the initiation and termination processes of earthquake rupture and its relation to morphology and geological structure. *Pure and Applied Geophysics*. https://doi.org/10.1007/BF00877216

Kurzon, I., Vernon, F. L., Ben-Zion, Y., & Atkinson, G. (2014). Ground Motion Prediction Equations in the San Jacinto Fault Zone: Significant Effects of Rupture Directivity and Fault Zone Amplification. *Pure and Applied Geophysics*. https://doi.org/10.1007/s00024-014-0855-2

Lewis, M. A., & Ben-Zion, Y. (2010). Diversity of fault zone damage and trapping structures in the Parkfield section of the San Andreas Fault from comprehensive analysis of near fault seismograms. *Geophysical Journal International*. https://doi.org/10.1111/j.1365-246X.2010.04816.x

Lewis, M. A., Peng, Z., Ben-Zion, Y., & Vernon, F. L. (2005). Shallow seismic trapping structure in the San Jacinto fault zone near Anza, California. *Geophysical Journal*

International. https://doi.org/10.1111/j.1365-246X.2005.02684.x

Li, Y. G., Leary, P., Aki, K., & Malin, P. (1990). Seismic trapped modes in the Oroville and San Andreas fault zones. *Science*. https://doi.org/10.1126/science.249.4970.763

Li, Y. G., Aki, K., Adams, D., Hasemi, A., & Lee, W. H. K. (1994). Seismic guided waves trapped in the fault zone of the Landers, California, earthquake of 1992. *Journal of Geophysical Research*. https://doi.org/10.1029/94jb00464

Mamada, Y., Kuwahara, Y., Ito, H., & Takenaka, H. (2004). Discontinuity of the Mozumi-Sukenobu fault low-velocity zone, central Japan, inferred from 3-D finite-difference simulation of fault zone waves excited by explosive sources. *Tectonophysics*. https://doi.org/10.1016/j.tecto.2003.09.008

Mitchell, T. M., Ben-Zion, Y., & Shimamoto, T. (2011). Pulverized fault rocks and damage asymmetry along the Arima-Takatsuki Tectonic Line, Japan. *Earth and Planetary Science Letters*. https://doi.org/10.1016/j.epsl.2011.04.023

Mizuno, T., Kuwahara, Y., Ito, H., & Nishigami, K. (2008). Spatial variations in fault-zone structure along the Nojima fault, central Japan, as inferred from borehole observations of fault-zone trapped waves. *Bulletin of the Seismological Society of America*. https://doi.org/10.1785/0120060247

Najdahmadi, B., Bohnhoff, M., & Ben-Zion, Y. (2016). Bimaterial interfaces at the Karadere segment of the North Anatolian Fault, northwestern Turkey. *Journal of Geophysical Research: Solid Earth*. https://doi.org/10.1002/2015JB012601

Ozakin, Y., Ben-Zion, Y., Aktar, M., Karabulut, H., & Peng, Z. (2012). Velocity contrast across the 1944 rupture zone of the North Anatolian fault east of Ismetpasa from analysis of teleseismic arrivals. *Geophysical Research Letters*. https://doi.org/10.1029/2012GL051426

Peng, Z., Ben-Zion, Y., Michael, A. J., & Zhu, L. (2003). Quantitative analysis of seismic fault zone waves in the rupture zone of the 1992 Landers, California, earthquake: Evidence for a shallow trapping structure. *Geophysical Journal International*. https://doi.org/10.1111/j.1365-246X.2003.02109.x

Qin, L., Ben-Zion, Y., Qiu, H., Share, P. E., Ross, Z. E., & Vernon, F. L. (2018). Internal structure of the san jacinto fault zone in the trifurcation area southeast of anza, california, from data of dense seismic arrays. *Geophysical Journal International*, *213*(1), 98–114. https://doi.org/10.1093/gji/ggx540

Qiu, H., Ben-Zion, Y., Ross, Z. E., Share, P. E., & Vernon, F. L. (2017). Internal structure of the San Jacinto fault zone at Jackass Flat from data recorded by a dense linear array. *Geophysical Journal International*, *209*(3), 1369–1388. https://doi.org/10.1093/gji/ggx096

Ross, Z. E., Idini, B., Jia, Z., Stephenson, O. L., Zhong, M., Wang, X., et al. (2019). 2019 Ridgecrest earthquake sequence. *Science*, *3665*(October), 346–351.

Rovelli, A., Caserta, A., Marra, F., & Ruggiero, V. (2002). Can seismic waves be trapped inside an inactive fault zone? The case study of Nocera Umbra, Central Italy. *Bulletin of the Seismological Society of America*. https://doi.org/10.1785/0120010288

Share, P. E., Ben-Zion, Y., Ross, Z. E., Qiu, H., & Vernon, F. L. (2017). Internal structure of the San Jacinto fault zone at Blackburn Saddle from seismic data of a linear array. *Geophysical Journal International*, *210*(2), 819–832. https://doi.org/10.1093/gji/ggx191

718 Share, P. E., Allam, A. A., Ben-Zion, Y., Lin, F.-C., & Vernon, F. L. (2019). Structural
719 Properties of the San Jacinto Fault Zone at Blackburn Saddle from Seismic Data of a
720 Dense Linear Array. *Pure and Applied Geophysics*, *176*(3), 1169–1191.
721 https://doi.org/10.1007/s00024-018-1988-5
722 Shlomai, H., & Fineberg, J. (2016). The structure of slip-pulses and supershear ruptures
723 driving slip in bimaterial friction. *Nature Communications*.
724 https://doi.org/10.1038/ncomms11787
725 Spudich, P., & Olsen, K. B. (2001). Fault zone amplified waves as a possible seismic
726 hazard along the Calaveras fault in central California. *Geophysical Research Letters*.
727 https://doi.org/10.1029/2000GL011902
728 Thakur, P., Huang, Y., & Kaneko, Y. (2020). Effects of Low-Velocity Fault Damage
729 Zones on Long-Term Earthquake Behaviors on Mature Strike-Slip Faults. *Journal of*
730 *Geophysical Research: Solid Earth*. https://doi.org/10.1029/2020JB019587
731 Vidale, J., Helmberger, D. V., & Clayton, R. W. (1985). Finite-difference seismograms
732 for SH waves. *Bulletin of the Seismological Society of America*.
733 Wang, Y., Allam, A. A., & Lin, F.-C. (2019). Imaging the Fault Damage Zone of the San
734 Jacinto Fault Near Anza With Ambient Noise Tomography Using a Dense Nodal
735 Array. *Geophysical Research Letters*. https://doi.org/10.1029/2019GL084835
736 Wechsler, N., Rockwell, T. K., & Ben-Zion, Y. (2009). Application of high resolution
737 DEM data to detect rock damage from geomorphic signals along the central San
738 Jacinto Fault. *Geomorphology*. https://doi.org/10.1016/j.geomorph.2009.06.007
739 Weertman, J. (1980). Unstable slippage across a fault that separates elastic media of
740 different elastic constants. *Journal of Geophysical Research*, *85*(B3), 1455–1461.
741 https://doi.org/10.1029/JB085iB03p01455
742 White, M. C., Fang, H., Catchings, R. D., Goldman, M. R., Steidl, J. H., & Ben-Zion, Y.
743 (2020, 07). Detailed traveltime tomography and seismicity around the 2019 M7.1
744 Ridgecrest, CA, earthquake using dense rapid-response seismic data . Poster
745 Presentation at 2020 SCEC Annual Meeting.
746 Xu, S., Ben-Zion, Y., & Ampuero, J. P. (2012). Properties of inelastic yielding zones
747 generated by in-plane dynamic ruptures-II. Detailed parameter-space study.
748 *Geophysical Journal International*. https://doi.org/10.1111/j.1365-
749 246X.2012.05685.x
750 Xu, X., Sandwell, D. T., & Smith-Konter, B. (2020). Coseismic displacements and
751 surface fractures from sentinel-1 InSAR: 2019 Ridgecrest earthquakes.
752 *Seismological Research Letters*, *91*(4), 1979–1985.
753 https://doi.org/10.1785/0220190275

754 Figure 1. Location map for the 2019 Ridgecrest earthquake sequence (colored
755 circles, square, and stars) and four linear arrays (B1, B2, B3, and B4 as red, green,
756 blue, and purple triangles, respectively) analyzed in this study. The catalog of
757 Hauksson et al. (2012, extended to 2019) is used for earthquake locations, with color
758 representing the focal depth (colorbar). The epicenters of 2019 Mw 6.4 and Mw 7.1
759 Ridgecrest earthquakes are marked as stars. Bandpass filtered waveforms, fault zone
760 head waves, and fault zone trapped waves of an example event (orange square)
761 recorded at array B4 are shown in Figs. S7, S8, and 7. Fault surface traces are
762 depicted as black lines with ruptures of the 2019 Ridgecrest earthquake sequence
763 being thicker. Seismic events outlined by the red box are analyzed in sections 3.2 and
764 3.3. The background gray colors indicate the local topography. WLSZ – Walker Lane
765 Shear Zone; ECSZ – Eastern California Shear Zone; EF – Elsinore Fault; GF –
766 Garlock Fault; SAF – San Andreas Fault; SJF – San Jacinto Fault.

767 Figure 2. Zoomed-in maps of the Ridgecrest linear arrays (triangles), B1-B4 in
768 (a)-(d), respectively. Color of the triangles represents the station elevation. The green
769 circle and black lines denote the center of the array and surface traces of faults
770 associated with the 2019 Mw 7.1 and Mw 6.4 Ridgecrest earthquakes (red and blue
771 stars, respectively), respectively. The red bar outlines the range of core damage zone
772 shown in Figure 6, identified in section 3.2; whereas, the green bar illustrates the span
773 of the entire low-velocity zone.

774 Figure 3. Teleseismic *P* waves recorded on vertical-component sensors of array
775 B4. (a). The top panel shows the locations of array B4 (triangle) and four analyzed
776 teleseismic events (stars), with the red star indicating the target event. The colormap
777 illustrates the teleseismic *P* waveforms recorded by the entire array B4, with red and
778 blue indicating positive and negative values. The *P*-wave arrival time predicted from
779 the model IASP-91 is used to align the *P* waveforms and is set to be zero in the time
780 axis. The *P* waveforms are bandpass filtered twice. After applying a bandpass filter
781 between 0.5 and 2 Hz, the array-mean envelope function and a preliminary *P*-wave
782 pick are computed and depicted as the curve and the vertical solid line in black.
783 Amplitude spectrum averaged over the entire array is calculated and shown in the

784 bottom left inset, with the red star and horizontal dashed lines indicating the peak
785 frequency and median of the amplitude spectrum between 0.5 and 2 Hz, respectively.
786 Then, a second bandpass filter between the frequency range outlined by the vertical
787 dashed lines in the bottom left inset is applied. The red dashed curves depict the
788 teleseismic *P*-wave delay times, measured using the *P* waveforms between the
789 vertical dashed lines ($\pm$ one dominant period relative to the preliminary *P*-wave
790 pick). (b)-(d) Same as (a) for the other three teleseismic events.

791 Figure 4. Teleseismic *P*-wave delay times for arrays (a) B1, (b) B2, (c) B3, and
792 (d) B4. The colored stars indicate *P*-wave delay times measured from different
793 teleseismic events and are labeled in the legend by the corresponding peak frequency
794 of the array-mean *P*-wave amplitude spectrum. The black dots depict the delay-time
795 pattern averaged over all teleseismic events, with error bars representing the standard
796 deviation of the mean. The blue and red dashed curves illustrate the delay times after
797 a topographic correction, assuming *P*-wave velocities of 2 km/s and 4 km/s.

798 Figure 5. (a) *P* waveforms of an example local seismic event, shown as the blue
799 star in (c), recorded on vertical-component sensors of array B1. Waveform at each
800 station is normalized by its corresponding maximum amplitude and bandpass filtered
801 between 0.5 and 20 Hz. Red stars denote the automatic *P* picks. (b) Same as (a) but
802 shown in slowness domain, i.e. the time axis of each station is normalized by the
803 corresponding hypocenter distance. Waveforms within the slowness window of 0.15
804 s/km and 0.25 s/km is used to exclude *S*-wave signals. (c) Distribution of seismic
805 events (colored circles) used in the local *P*-wave delay-time analysis for array B1 (red
806 triangles). The black lines and gray dots represent fault surface traces and earthquakes
807 that are excluded from the delay-time analysis in section 3.2.

808 Figure 6. Statistical analysis of local *P*-wave arrival patterns. (a) Red dots
809 illustrate the *P*-wave relative-slowness variation within array B1, averaged over 670
810 local seismic events (colored dots in Fig. 5c), with error bars representing a range of
811 two standard deviations about each respective mean value. The histogram of relative
812 slowness values obtained at each station for all analyzed events is illustrated as the
813 background gray colors (colorbar). The solid black lines depict the contribution

associated with the *P*-wave velocity contrast (~4.6%) across the fault beneath array B1. PDF – Probability Density Function. (b) Same as (a) for variations in the local-structure-related *P*-wave travel times (Equation 3) across array B1. Similar mean delay pattern (red curve) is observed, with *P* waves being ~0.1 s slower in the southwest than the northeast. The red dashed vertical lines outline an ~500-m-wide core damage zone (red bars in Fig. 2a) that delays *P* waves by ~0.055 s with respect to the black curve, whereas the entire range of the low-velocity zone (green bar in Fig. 2a) is bounded by the green dashed vertical lines. For results of arrays B2, B3, and B4, (c)-(d), (e)-(f), and (g)-(h), respectively, are the same as (a)-(b).

Figure 7. (a) Fault zone trapped waves (FZTWs) following the *S*-wave arrivals for an example event (square in Fig. 1) observed at the fault-parallel component of array B4. The waveforms are preprocessed following the steps of Figure S6 of Qiu et al. (2017), i.e. remove instrument response, bandpass filter between 2 and 20 Hz, integrate velocity to displacement seismograms, and convolve with $1/t^{1/2}$. The blue bar outlines the stations with FZTW. (b) Red dots and blue stars denote the distributions of normalized peak ground velocities (PGV) and root mean squares (RMS) of the *S* waveforms shown in (a). The black curve represents the likelihood of FZTW that is the normalized multiplication of PGV and RMS values and is used to identify FZTW candidates.

Figure 8. (a) Histograms of FZTW-likelihood values computed for each station in array B1 over all analyzed events (background gray colors). Red dots indicate the mean likelihood values of FZTWs (black curve in Fig. 7b) averaged over all analyzed events. Error bars represent a range of two standard deviations about each respective mean value. The top red and bottom blue bars mark the zones of high mean FZTW-likelihood values (> 0.4) and core damage zone identified from local *P*-wave delay-time analysis (red dashed lines in Fig. 6b), respectively. (b)-(d) Same as (a) for results of arrays B2, B3, and B4, respectively.

Figure 9. (a) Locations of earthquakes (gray dots) analyzed in section 3.3. FZTW candidates identified through waveform cross correlations, with cross correlation coefficient greater than 0.85 marked as stars and color representing the focal depth.

Red triangles denote the location of array B4. The along-fault cross section of seismicity (dots and stars) and array B4 (triangle) are shown in the top inset. (b) FZTW recorded at stations B416-B423 for nine high-quality candidate events (red) with the highest correlation coefficients. The template waveforms (Fig. 7a) are shown in black. The array-mean *S* pick and cross correlation coefficient of each candidate event are labeled in the top left. (c) Comparison between FZTW of the reference event (in black) and those averaged over all the high-quality candidate events (in red) observed between stations B416-B423.

Figure 10. Inversion results for FZTW observed between stations B416-423, averaged over candidates shown in Figure 9a. (a) Comparison between synthetic waveforms (red) computed using the best-fitting model parameters (black dots in (b)) and the observed FZTW (in black). (b) Fitness values of fault-zone model parameters from the last 10 generations of the inversion (green dots). The best-fitting parameters (black circles) are displayed in each panel and used to generate the synthetic waveforms shown in (a). Black curve indicates probability density of model parameters shown as green dots.

Figure 11. (a) Stars illustrate the events that show strong fault-zone reflected *P* waves (FZRWs) at array B4 (red triangles). Velocity contrast across the fault beneath array B4, resolved from delay-time analyses in sections 3.1 and 3.2 is labeled. (b) Vertical-component waveforms of the M 2.6 event marked as the circle in (a) recorded at array B4. The red and blue dashed curves indicate the preliminary *P* and *S* picks, respectively. The strong FZRWs are highlighted by the green curve, whereas the red vertical bar delineates the group of stations that recorded clear FZTWs (e.g., blue bar in Fig. 7a). Polarity of the direct *P* waves are illustrated by the red (positive) and blue (negative) arrows, whereas stations outlined by the black arrow are close to the focal plane and yield weak *P* arrivals. (c) Three-component waveforms recorded at station B431. Direct *P* wave, FZRW, and *S* wave are labeled.

Figure 12. (a) Google Earth photo of the Ridgecrest region. Red circles denote the four linear arrays, B1-B4. The velocity contrasts across fault and low-velocity zones inferred from local *P*-wave delay time analysis (Fig. 6) are labeled in the text and

874 marked as thick green and red bars, respectively. Stations that show FZTWs (Figs. 7a
875 and S9b) and FZHWs (Figs. S8 and S9a) are marked as thin blue solid lines and red
876 dashed lines, respectively, with arrow pointing towards the slow side. The black thick
877 lines indicate fault surface traces of the 2019 Mw 6.4 and Mw 7.1 Ridgecrest
878 earthquakes, whereas the light black lines and background colors illustrate the surface
879 displacements and distribution of rock types in the Ridgecrest region obtained from
880 Jennings et al. (1977). (b) Histogram of array-mean *P*-wave velocities computed in
881 section 3.2 for all source-array pairs. (c) Fault normal cross section beneath array B4
882 (triangles). Earthquakes with FZRWs (stars in Fig. 11a) are marked as colored stars
883 and circle. The polarity of *P*-wave first motion, separated by the focal plane (black
884 dashed lines), is positive at stations within the red arrow and negative inside the blue
885 arrow for the example event (circle). Schematic propagation paths for direct *P* waves
886 and FZRWs recorded by station B431 are depicted in red (positive polarity) and blue
887 (negative polarity). The red and blue bars highlight stations with FZTWs (Fig. 7a)
888 and inside the core damage zone identified in Figure 6h, respectively. The black line
889 northeast to the red bar depicts the damage zone boundary that produces FZHW (Fig.
890 S8). Stations with clear FZRWs (green curve in Fig. 11b) for the example event
891 (circle) are marked as green triangles. The schematic ray path in green denotes the
892 propagation of FZRWs to the green station with the largest fault normal distance, and
893 its reflection point likely indicates the depth (~4 km) of the reflection interface (black
894 line SW to the red bar).

Figure 1.

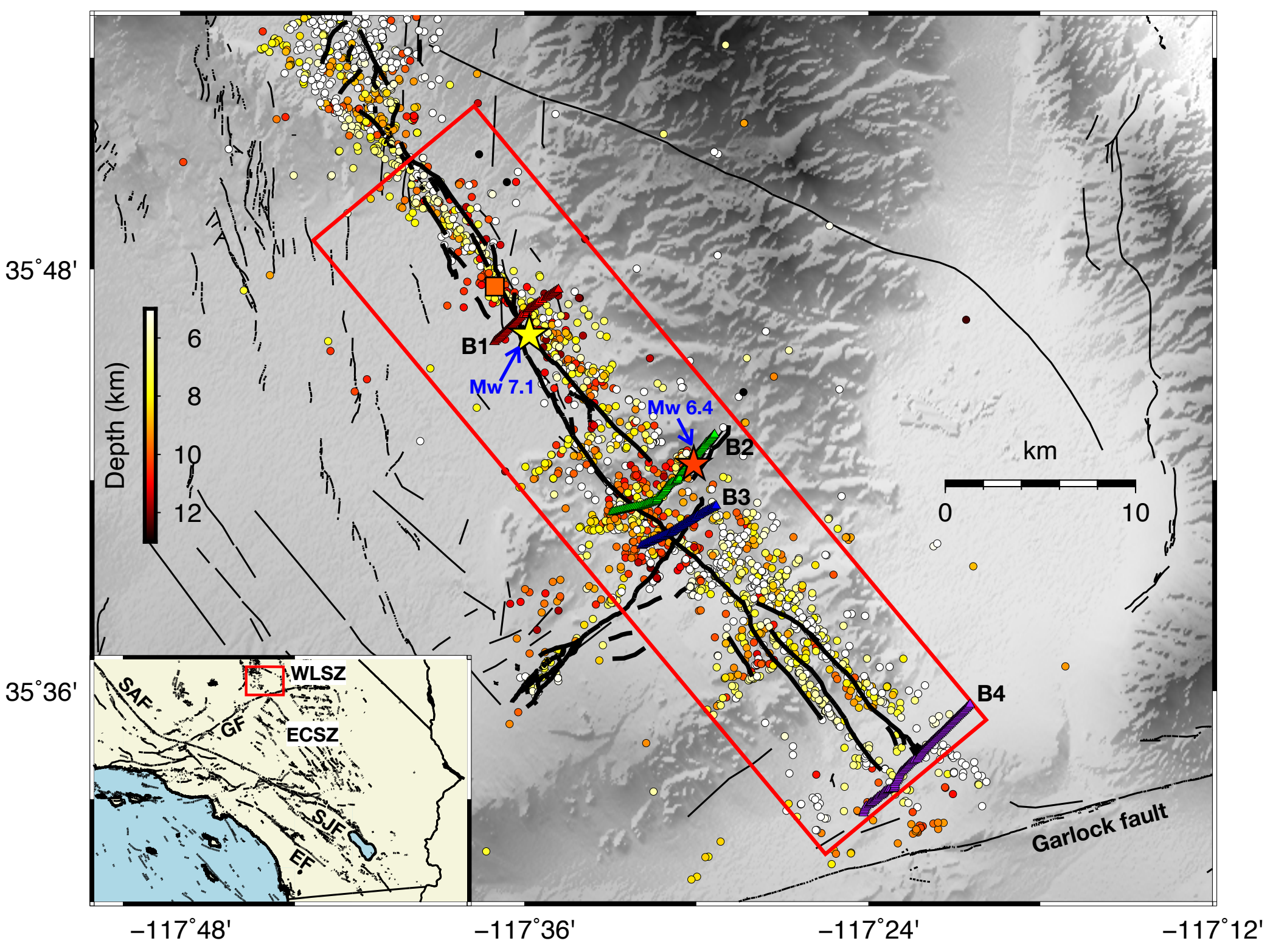
35˚48'
35˚36'
−117˚48'
−117˚36'
−117˚24'
−117˚12'
Depth (km)
6
8
10
12
B1
Mw 7.1
Mw 6.4
B2
B3
B4
km
0
10
Garlock fault
WLSZ
SAF
GF
ECSZ
SJF
EF

Figure 2.

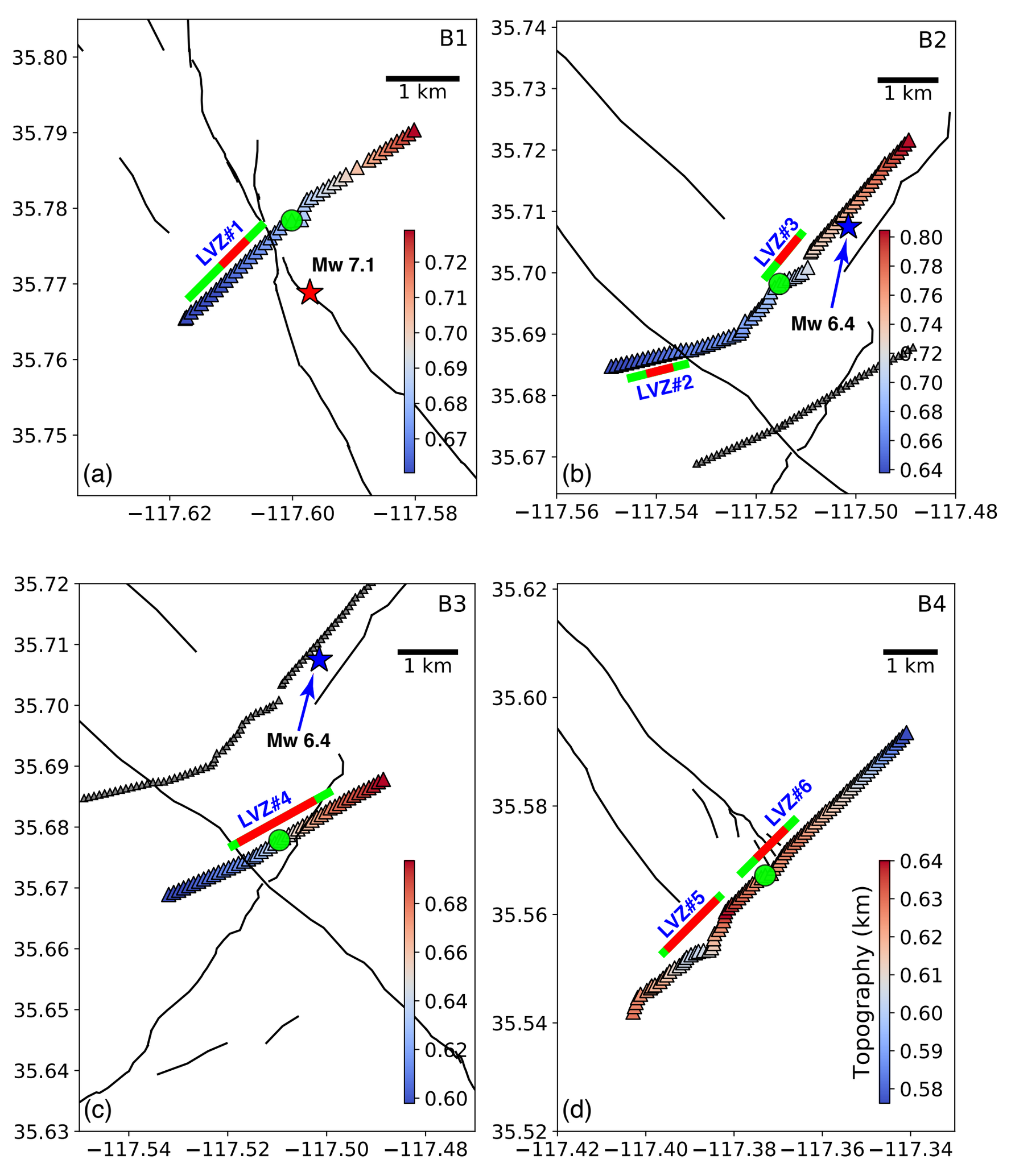
B1
1 km
LVZ#1
Mw 7.1
(a)
B2
1 km
LVZ#3
LVZ#2
Mw 6.4
(b)
B3
1 km
Mw 6.4
LVZ#4
(c)
B4
1 km
LVZ#6
LVZ#5
Topography (km)
(d)

Figure 3.

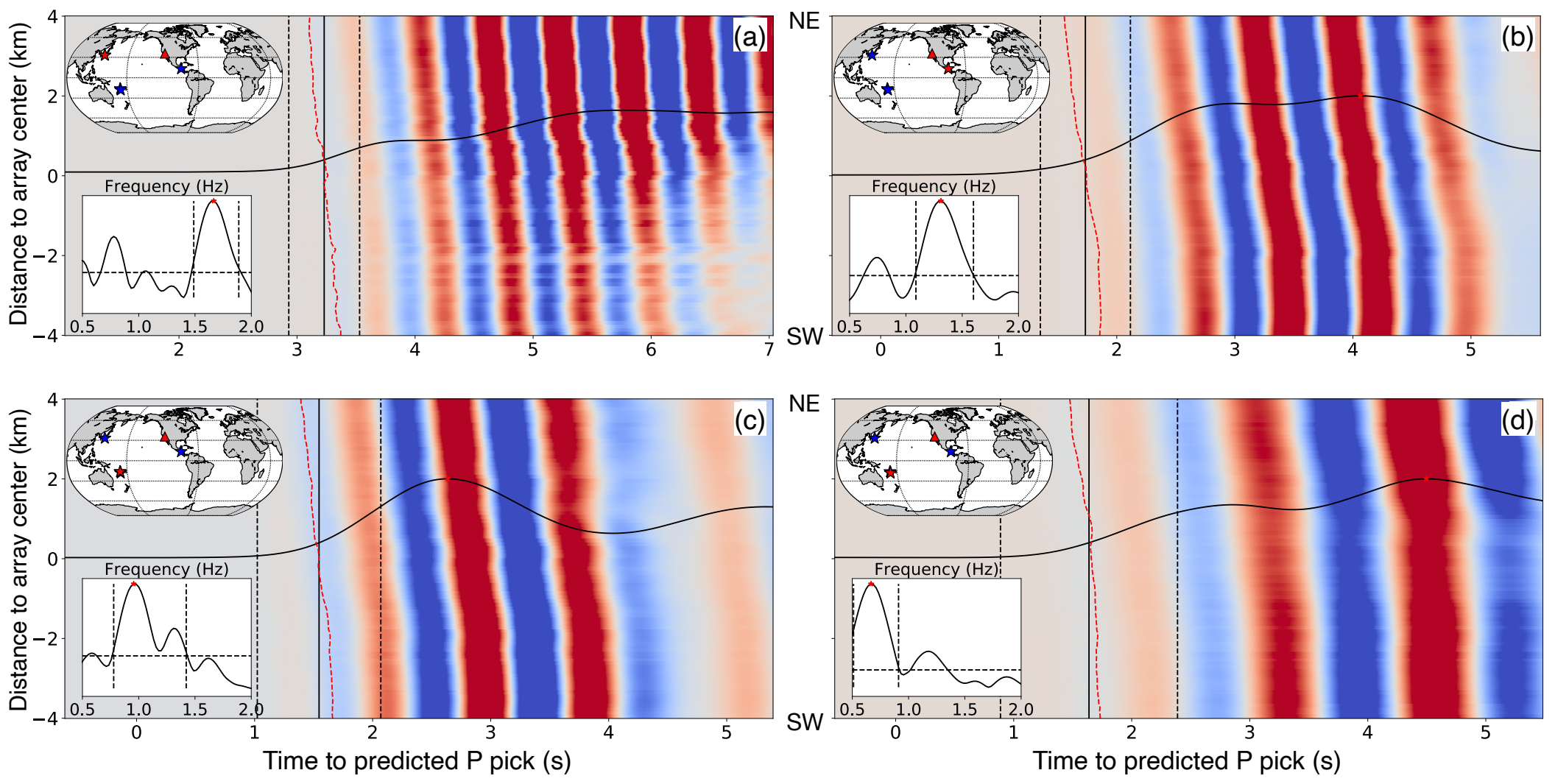
(a)
(b)
(c)
(d)
NE
SW
Distance to array center (km)
Time to predicted P pick (s)
Frequency (Hz)

Figure 4.

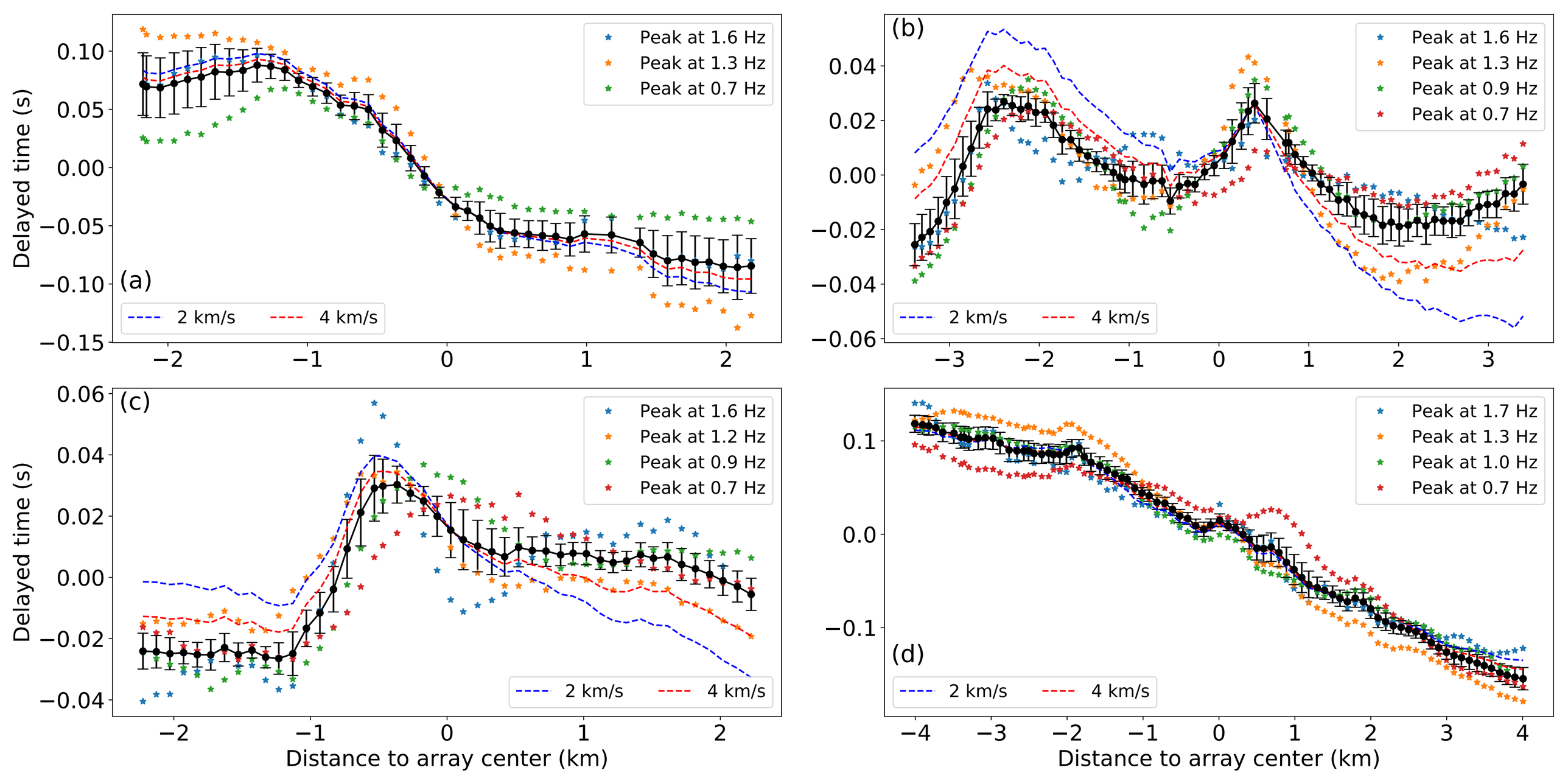
(a)
Peak at 1.6 Hz
Peak at 1.3 Hz
Peak at 0.7 Hz
2 km/s
4 km/s
Delayed time (s)
(b)
Peak at 1.6 Hz
Peak at 1.3 Hz
Peak at 0.9 Hz
Peak at 0.7 Hz
2 km/s
4 km/s
(c)
Peak at 1.6 Hz
Peak at 1.2 Hz
Peak at 0.9 Hz
Peak at 0.7 Hz
2 km/s
4 km/s
Delayed time (s)
Distance to array center (km)
(d)
Peak at 1.7 Hz
Peak at 1.3 Hz
Peak at 1.0 Hz
Peak at 0.7 Hz
2 km/s
4 km/s
Distance to array center (km)

Figure 5.

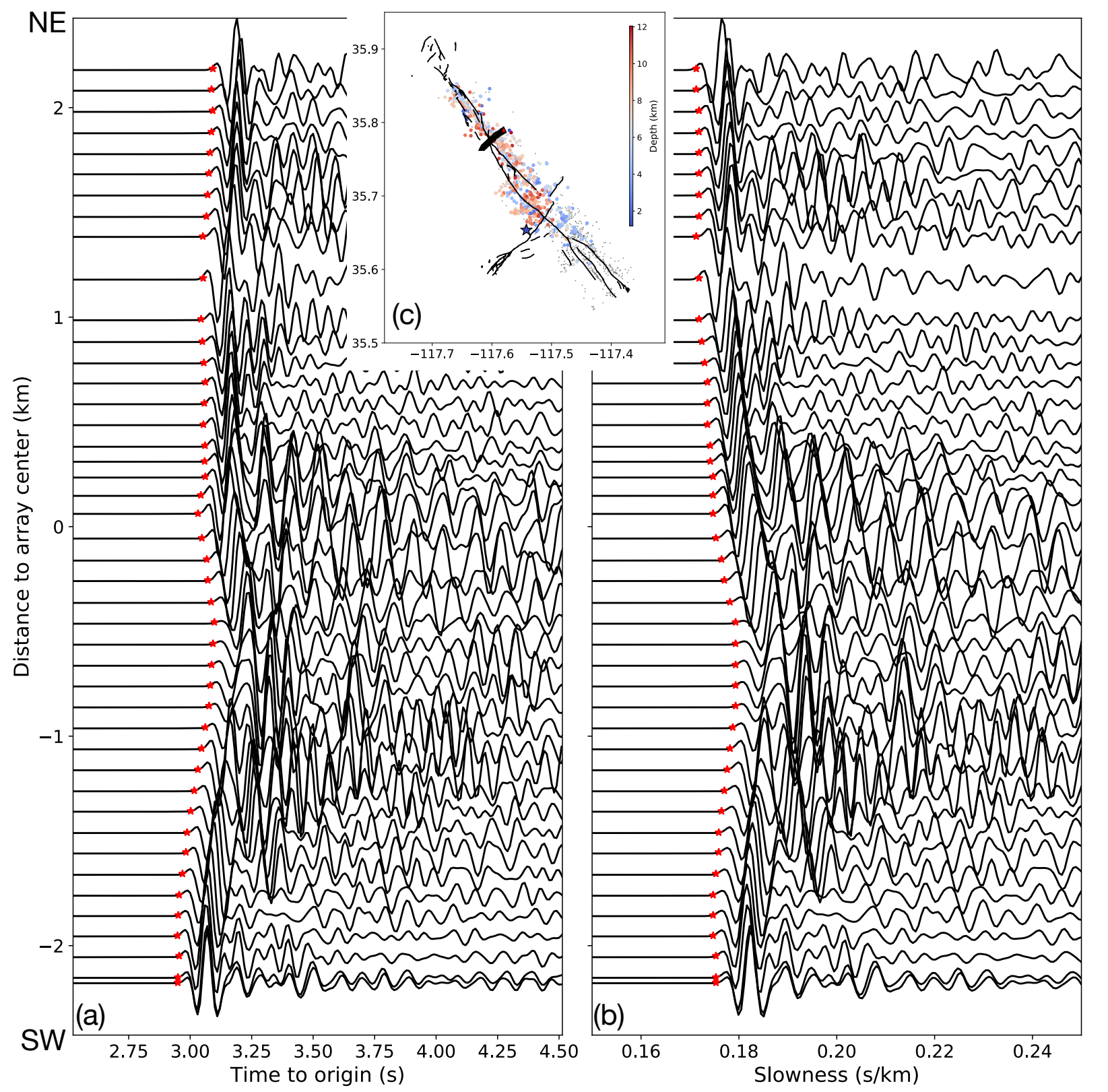
NE
SW
Distance to array center (km)
2
1
0
−1
−2
(a)
(b)
(c)
Time to origin (s)
2.75
3.00
3.25
3.50
3.75
4.00
4.25
4.50
Slowness (s/km)
0.16
0.18
0.20
0.22
0.24
35.9
35.8
35.7
35.6
35.5
−117.7
−117.6
−117.5
−117.4
Depth (km)
12
10
8
6
4
2

Figure 6.

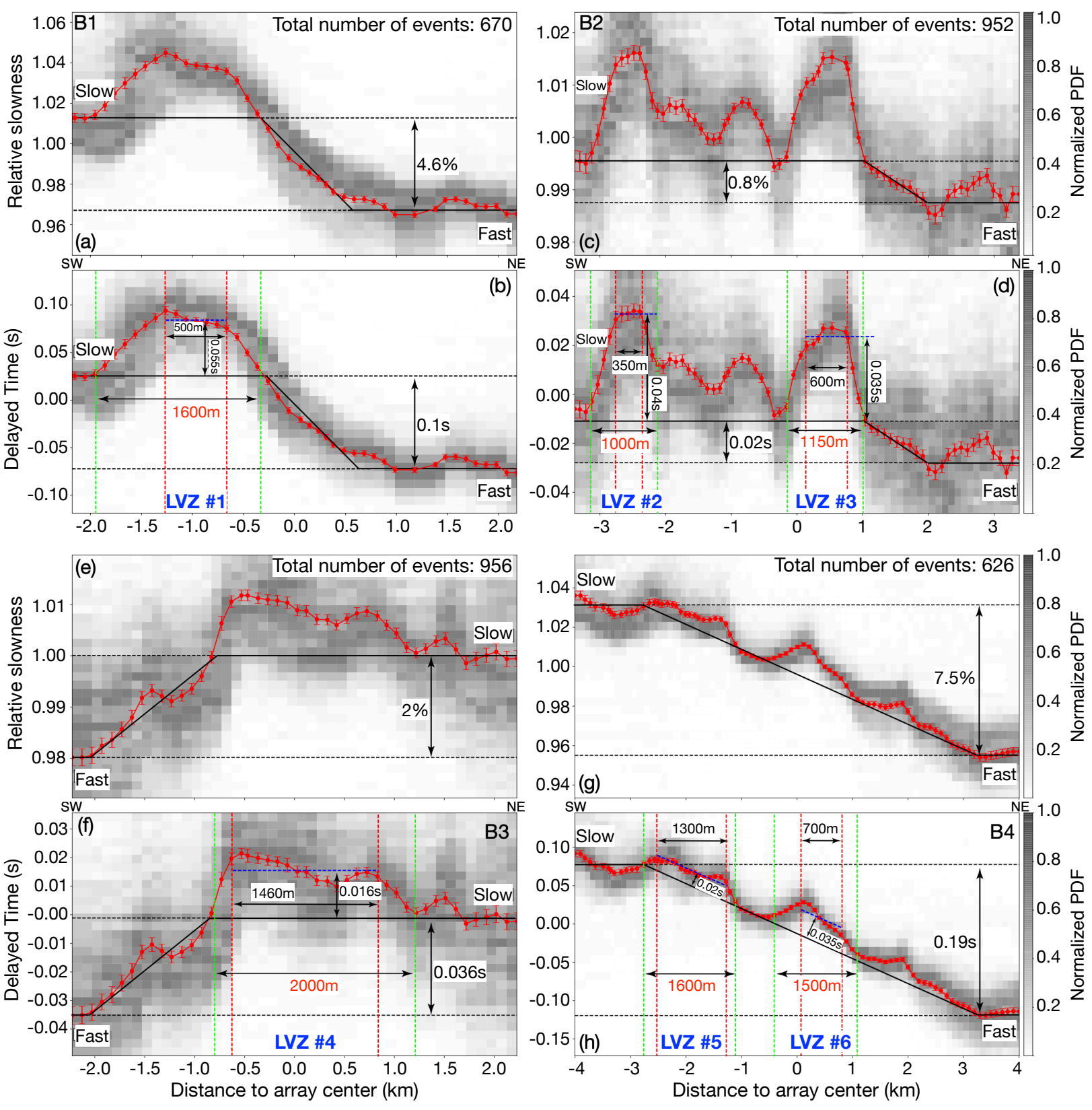
B1
Total number of events: 670
Slow
4.6%
Fast
(a)
B2
Total number of events: 952
Slow
0.8%
Fast
(c)
Relative slowness
Normalized PDF
SW
NE
(b)
Slow
500m
0.055s
1600m
0.1s
Fast
LVZ #1
(d)
Slow
350m
0.04s
1000m
0.02s
600m
0.035s
1150m
Fast
LVZ #2
LVZ #3
Delayed Time (s)
(e)
Total number of events: 956
Slow
2%
Fast
Total number of events: 626
Slow
7.5%
Fast
(g)
(f)
B3
1460m
0.016s
Slow
2000m
0.036s
Fast
LVZ #4
B4
Slow
1300m
700m
0.02s
0.035s
0.19s
1600m
1500m
Fast
(h)
LVZ #5
LVZ #6
Distance to array center (km)

Figure 7.

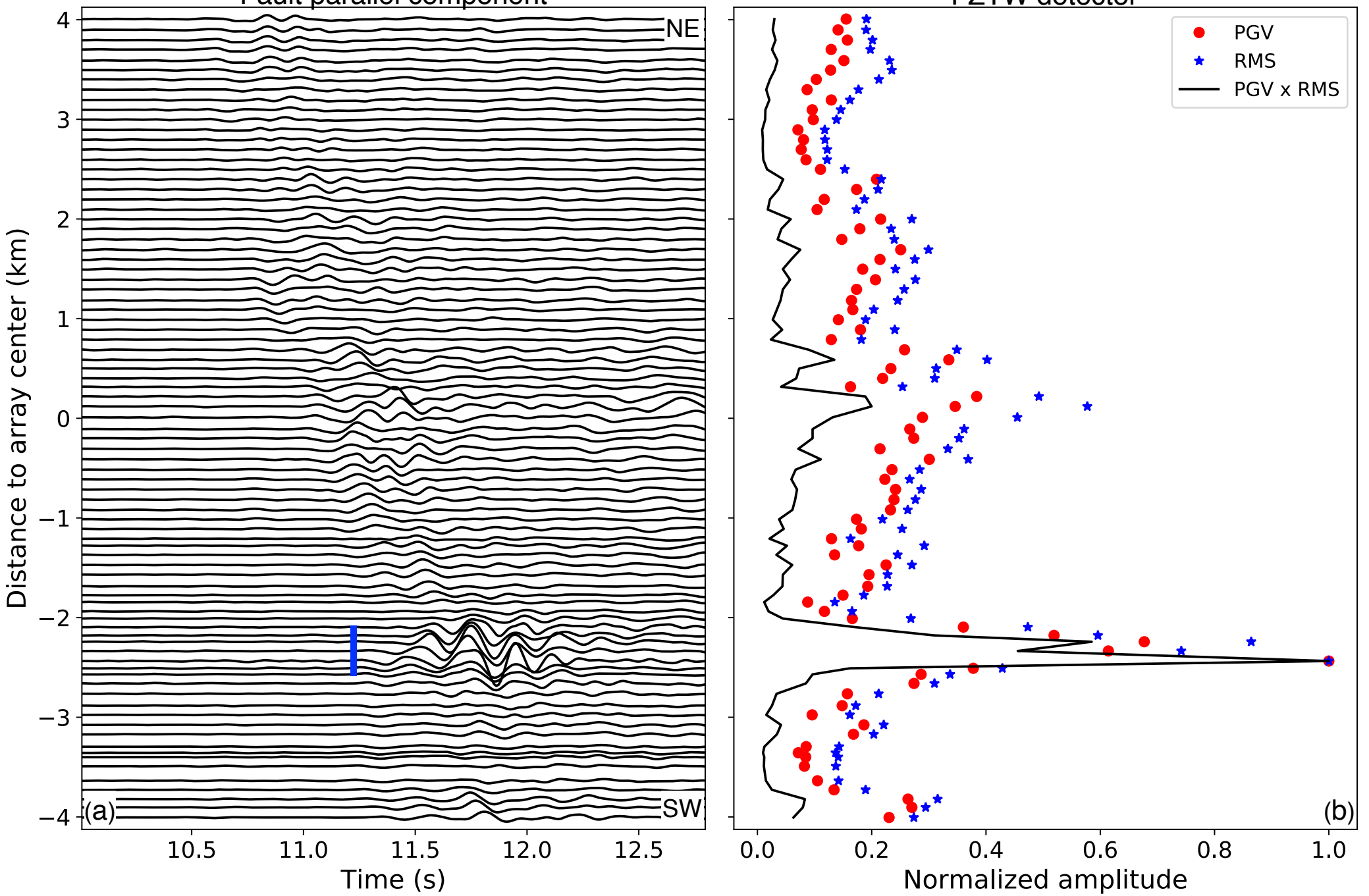
Fault parallel component
FZTW detector
NE
SW
(a)
(b)
Distance to array center (km)
Time (s)
Normalized amplitude
PGV
RMS
PGV x RMS
4
3
2
1
0
−1
−2
−3
−4
10.5
11.0
11.5
12.0
12.5
0.0
0.2
0.4
0.6
0.8
1.0

Figure 8.

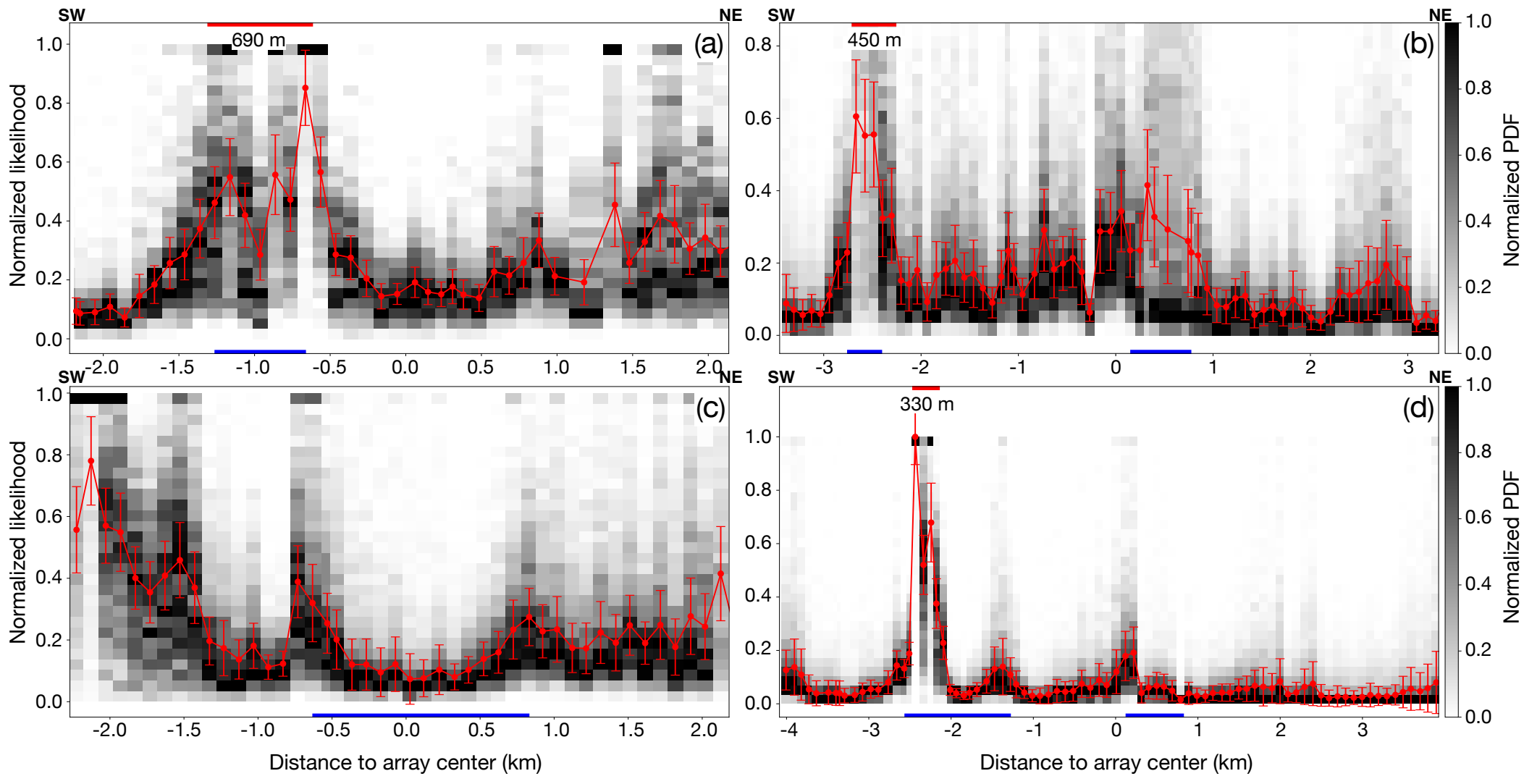
SW
NE
690 m
(a)
Normalized likelihood
450 m
(b)
Normalized PDF
(c)
330 m
(d)
Distance to array center (km)

Figure 9.

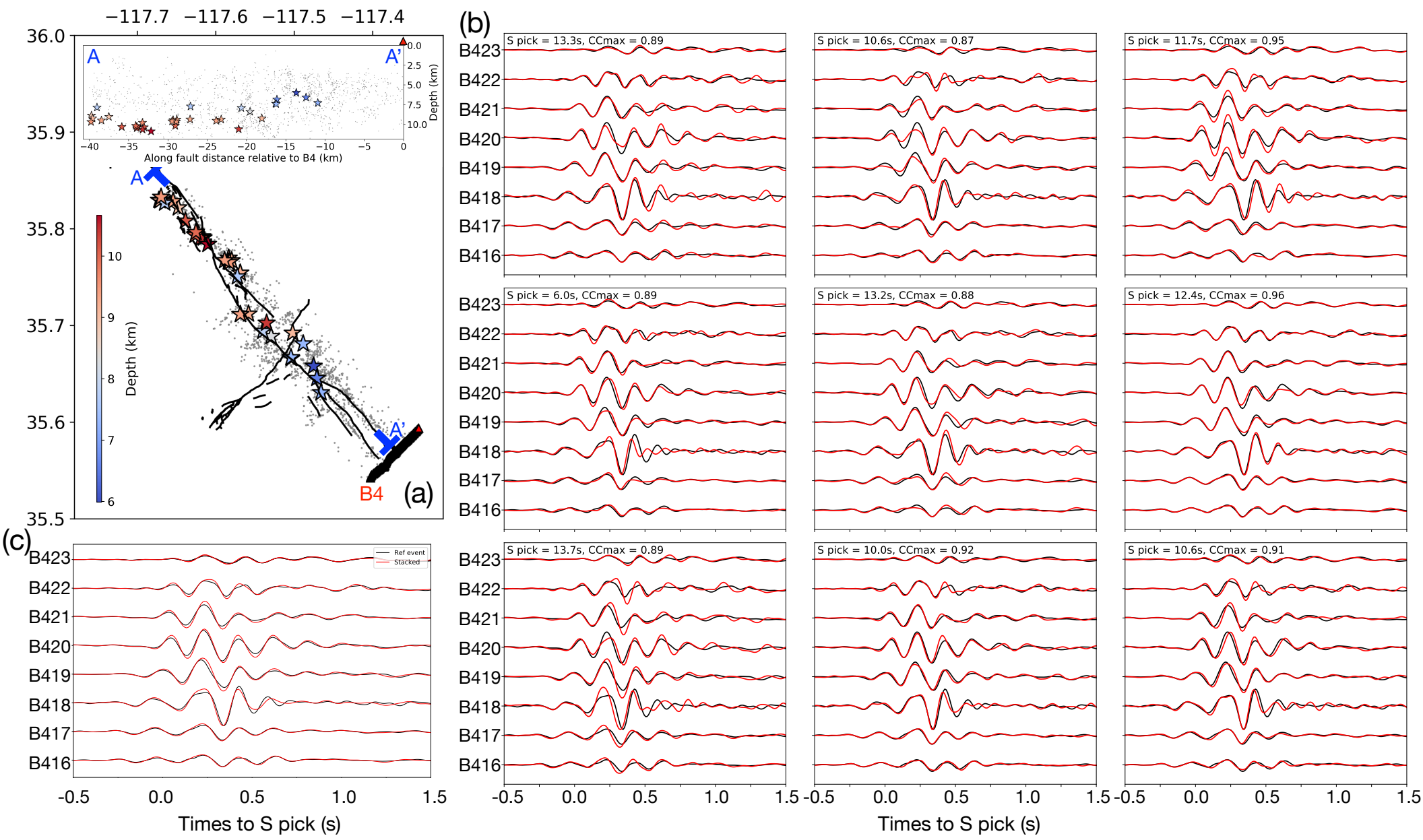
(a)
(b)
(c)
A
A'
B4
Depth (km)
Along fault distance relative to B4 (km)
−117.7 −117.6 −117.5 −117.4
36.0
35.9
35.8
35.7
35.6
35.5
B423
B422
B421
B420
B419
B418
B417
B416
S pick = 13.3s, CCmax = 0.89
S pick = 10.6s, CCmax = 0.87
S pick = 11.7s, CCmax = 0.95
S pick = 6.0s, CCmax = 0.89
S pick = 13.2s, CCmax = 0.88
S pick = 12.4s, CCmax = 0.96
S pick = 13.7s, CCmax = 0.89
S pick = 10.0s, CCmax = 0.92
S pick = 10.6s, CCmax = 0.91
Ref event
Stacked
Times to S pick (s)
Times to S pick (s)

Figure 10.

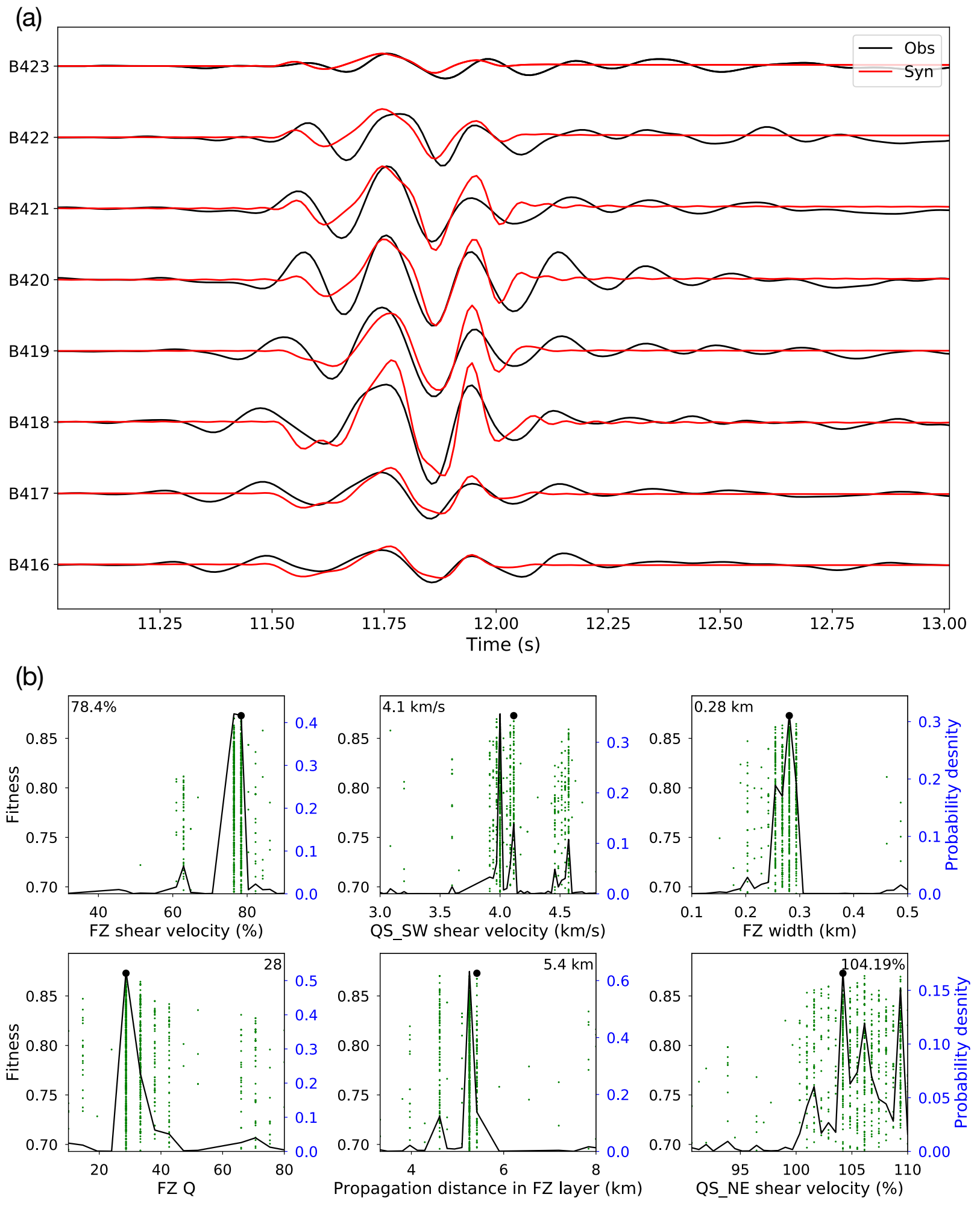
(a)
B423
B422
B421
B420
B419
B418
B417
B416
Obs
Syn
11.25
11.50
11.75
12.00
12.25
12.50
12.75
13.00
Time (s)
(b)
78.4%
4.1 km/s
0.28 km
28
5.4 km
104.19%
Fitness
Probability desnity
FZ shear velocity (%)
QS_SW shear velocity (km/s)
FZ width (km)
FZ Q
Propagation distance in FZ layer (km)
QS_NE shear velocity (%)

Figure 11.

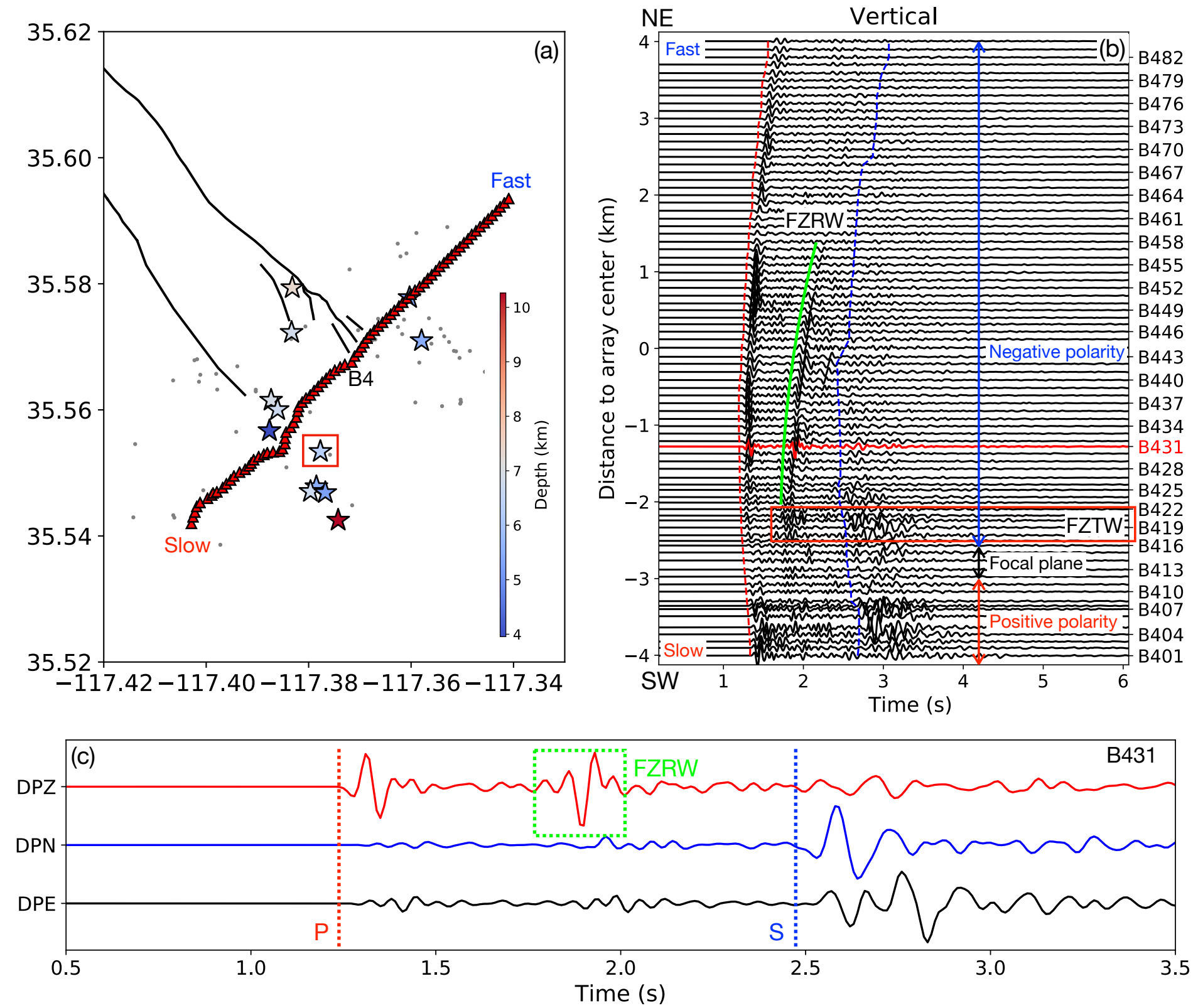
(a)
Fast
Slow
B4
Depth (km)
35.62
35.60
35.58
35.56
35.54
35.52
−117.42
−117.40
−117.38
−117.36
−117.34
NE
Vertical
(b)
Fast
FZRW
Negative polarity
FZTW
Focal plane
Positive polarity
Slow
SW
Distance to array center (km)
Time (s)
B482
B479
B476
B473
B470
B467
B464
B461
B458
B455
B452
B449
B446
B443
B440
B437
B434
B431
B428
B425
B422
B419
B416
B413
B410
B407
B404
B401
(c)
B431
DPZ
DPN
DPE
FZRW
P
S
Time (s)

Figure 12.

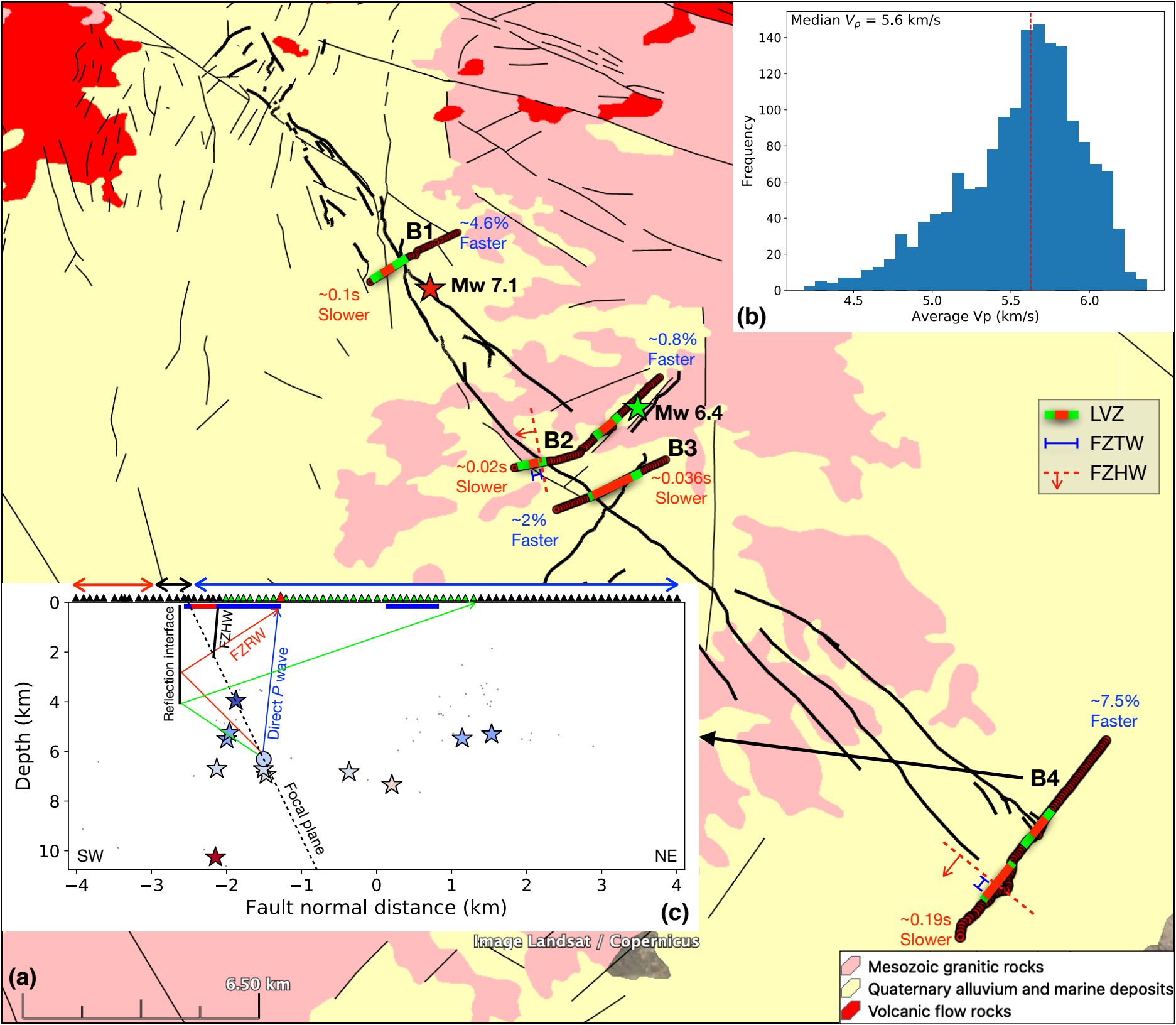
Median V_p = 5.6 km/s
Frequency
Average Vp (km/s)
(b)
B1
~4.6%
Faster
~0.1s
Slower
Mw 7.1
~0.8%
Faster
Mw 6.4
B2
B3
~0.02s
Slower
~0.036s
Slower
~2%
Faster
LVZ
FZTW
FZHW
~7.5%
Faster
B4
~0.19s
Slower
Reflection interface
FZHW
FZRW
Direct P wave
Focal plane
SW
NE
Depth (km)
Fault normal distance (km)
(c)
Image Landsat / Copernicus
(a)
6.50 km
Mesozoic granitic rocks
Quaternary alluvium and marine deposits
Volcanic flow rocks